Role for Eurasian Arctic shelf sea ice in a secularly varying hemispheric climate signal during the 20^{th} century

By **Marcia Glaze Wyatt**[1] **and Judith A. Curry**[2]

16 September 2013

Accepted by *Climate Dynamics*

Abstract: A hypothesized low-frequency climate signal propagating across the Northern Hemisphere through a network of synchronized climate indices was identified in previous analyses of instrumental and proxy data. The tempo of signal propagation is rationalized in terms of the multidecadal component of Atlantic Ocean variability – the Atlantic Multidecadal Oscillation. Through multivariate statistical analysis of an expanded database, we further investigate this hypothesized signal to elucidate propagation dynamics. The Eurasian Arctic Shelf-Sea Region, where sea ice is uniquely exposed to open ocean in the Northern Hemisphere, emerges as a strong contender for generating and sustaining propagation of the hemispheric signal. Ocean-ice-atmosphere coupling spawns a sequence of positive and negative feedbacks that convey persistence and quasi-oscillatory features to the signal. Further stabilizing the system are anomalies of co-varying Pacific-centered atmospheric circulations. Indirectly related to dynamics in the Eurasian Arctic, these anomalies appear to negatively feed back onto the Atlantic's freshwater balance. Earth's rotational rate and other proxies encode traces of this signal as it makes its way across the Northern Hemisphere.

Keywords: synchronized network · Arctic sea ice· multidecadal variability · climate regime

[1] Department of Geologic Sciences, CIRES/INSTAAR, Benson Earth Sciences Building, University of Colorado-Boulder, Boulder, CO 80309, USA e-mail: marciawyatt@earthlink.net

[2] School of Earth and Atmospheric Sciences, Georgia Institute of Technology, Atlanta, Georgia, USA.

1. Introduction

Behavior of numerous and diverse geophysical indices – from fish populations to cosmic nuclides – fluctuate at a quasi-periodic 50-to-80 year tempo (e.g. Ogurtsov et al. 2002; Patterson et al. 2004; Klyashtorin and Lyubushin 2007). Motivated by this ubiquity of tempo, Wyatt et al. (2012; hereafter WKT) analyzed 20th-century indices in the context of a hemispherically spanning climate network through which a signal propagates. WKT termed this propagating signal the 'stadium-wave' – an allusion to sections of sports fans seated in a stadium, standing and sitting as a 'wave' propagates through the audience. In like manner, a signal 'wave' appears to propagate through a hemispheric climate network.

Wyatt (2012) further explored the 'stadium-wave' signal, both spatially and temporally expanding the network. A 300-year proxy record revealed a hemispherically propagating signal, albeit with modifications of amplitude and tempo prior to the late 1700s. Wyatt and Peters (2012; hereafter WP) analyzed networks of indices reconstructed from model-simulated data generated by a suite of models in the third Coupled Model Intercomparison Project (CMIP3) using 20th century and pre-industrial forcings. No secularly varying, hemispherically propagating signal was found in the model simulations.

The stadium-wave signature identified in instrumental and proxy data is characterized by two leading modes of variability that together capture the spatio-temporal nature of the hemispherically spanning signal. WKT invoked numerous observational and model-based studies to support suggested physical dynamics potentially conveying connectivity within the stadium-wave network. Candidate mechanisms include low-frequency geographical shifts in oceanic and atmospheric mid-latitude centers-of-action and meridional displacements of ocean-gyre frontal boundaries (western-boundary-current extensions), from which ocean-heat flux to the atmosphere has the potential to influence overlying jet-stream behavior at decadal timescales. While modeling of interactions between individual components provides insight into potential localized coupling within the climate network, interaction between individual components is not the same as collective interaction, where a change in one network component or interaction promotes changes in all other network members and interactions among them. Recognizing this fundamental trait of network behavior (Pikovsky et al. 2001), WP hypothesized that failure to find the signal in any of the CMIP-model simulations might reflect the absence or poor representation of network dynamics fundamental to signal propagation. WP also discussed CMIP-modeling deficiencies in representing magnitude, configuration, and geographical displacements of the rather complex Arctic high-pressure system, a significant factor in simulating sea ice growth, extent and related dynamics (Gudkovich et al. 2008; Kwok 2011).

This paper extends WKT by investigating the underlying physical mechanisms associated with the stadium wave through analysis of an expanded network of geophysical indices, with particular focus on the Arctic region. Proxy indices are introduced to provide further insight into the multiple dynamics related to hemispheric signal propagation, such as migration of the Intertropical Convergence Zone, basin-scale wind patterns, western-boundary-current dynamics, and Arctic sea ice processes. Establishing proxy-process relationships connotes their potential use in extending the record prior to the 20th century. The expanded index collection provides insight and perspective on attribution and potential predictive capacity of the stadium wave.

2 Data and Methods

2.1 Data

We evaluate network (collective) behavior of geophysical indices, following WKT and WP. All newly added indices are discussed below and summarized details and index references are listed in **Table 1**. See WKT for descriptions of and references for original indices.

Original indices: Indices used in the original WKT stadium-wave analysis are also used in the present study. These indices include 20th-century instrumental values of well-known indices, such as the Northern Hemisphere area-averaged surface temperature (NHT), the Atlantic Multidecadal Oscillation (AMO), the North Atlantic Oscillation (NAO), an index representative of the El Nino-Southern Oscillation (NINO3.4), the North Pacific Oscillation (NPO), the Pacific Decadal Oscillation (PDO), the Aleutian Low Pressure Index (ALPI), and the less well-known index of Atmospheric-Mass-Transfer anomalies (AT: Vangenheim (1940); Girs (1971a)).

Long used in Russian studies, AT reflects atmospheric-pressure 'topography' that is used to assess whether the general direction of large-scale wind-flow patterns at mid-to-high latitudes (30ºN to 80ºN) of the Atlantic-Eurasian sector is zonal or meridional. Direction of cyclonic and anticyclonic air-mass transfers between 45ºE and 75ºE is evaluated daily from atmospheric-pressure maps. Anomalies relative to a long-term annual mean number-of-days that are characterized by dominantly zonal or meridional flow are tabulated for the year. The resulting AT time series, available since 1891, reflects negative meridional values, whereby positive values of AT indicate anomalous zonal flow (see Klyashtorin and Lyubushin 2007).

Indices of the original WKT index network were annually sampled. When available, boreal winter values were used - December, January, February, and March (DJFM) – when atmospheric variability is most intense and atmospheric modes are most pronounced.

Arctic indices: We have added the winter Arctic Oscillation (AO; Thompson and Wallace 2000) to our data set to augment our insight into the stratospheric-tropospheric coupling that occurs within the polar vortex during winter months. Variations in latitudinal distribution of atmospheric mass are associated with the AO, which represents the dominant pattern of non-seasonal sea-level-pressure (SLP) variations north of 20ºN. SLP and the associated atmospheric-mass shifts give insight into anomalies of cyclonicity or anti-cyclonicity at high latitudes – features that impact dynamics of atmosphere, sea ice, and ocean.

Arctic processes, particularly those in the Eurasian Arctic Shelf Seas, exhibit variability on timescales analogous to that of the stadium-wave signal. To examine whether there is a low-frequency relationship between Arctic processes and the propagating signal, we incorporate into our expanded network the annual mean Arctic surface air temperature (ArcT (70ºN to 85ºN) Frolov et al. 2009) and August mean values of the Eurasian Arctic sea ice extent (1900-2008: Frolov et al. 2009). These data are based on Russian sea ice charts (1933 to 2006: Arctic and Antarctic Research Institute (AARI)) and archival records, both compiled by the AARI. These data, digitized and available since 2006 (see Frolov et al. 2009 for full discussion and references within), have complete records for at least the 20th century for all the Eurasian Shelf Seas for the month of August, when seasonal ice is close to its annual minimum. The region considered here lies between 15ºW eastward to 155ºW. From west-to-east these seas are: the Greenland, Barents, Kara, Laptev, East Siberian, and Chukchi Seas (**Figure 1**).

Russian terminology groups these six seas into two categories according to shared seasonal characteristics: i) the North European Basin (NEB), comprised of the Greenland and Barents Seas, is distinguished by the fact that portions of the region remain ice free during winter and interannual variability of ice extent is not confined to summer; ii) the Arctic Seas of Siberia (ArcSib), which includes the Kara, Laptev, East Siberian, and Chukchi Seas, typically remains mostly ice-covered throughout the winter, interannually varying only in the summer. Summer melt strongly influences sea-ice thickness the following winter, and by extension, governs extent of ocean-heat flux through the ice cover to the overlying atmosphere during those months when ocean's influence on the atmosphere at high latitudes is greatest.

We further sort these seas according to dominant frequency of variability to elucidate impact of timescale: i) the West Eurasian Seas (West Ice Extent (WIE)) exhibit a pronounced 50-to-80-year tempo of sea-ice-extent variability and include the Greenland, Barents, and Kara Seas; while ii) the East Eurasian Seas (East Ice Extent (EIE)), which include the Laptev, East Siberian, and Chukchi Seas, are dominated by interannual-to-interdecadal timescales of variability: 20-to-30 years and eight-to-ten years. These higher frequencies are superimposed upon a weak multidecadal component in EIE. Combined normalized values of WIE and EIE equal the total ice extent (TIE) of the Eurasian Arctic Seas (**Table 2**).

Atlantic-Eurasian and Pacific circulation indices: Decadal-scale anomaly trends of Atlantic-Eurasian atmospheric circulation (i.e. AT), are captured in the Atmospheric Circulation Index (ACI (aka Vangenheim-Girs Index): Girs 1971a; Beamish 1998). ACI is the time-integral curve of AT anomalies (aka cumulative-sum of AT (csAT)). Trend reversals of the anomaly trends, or change points, have been linked to decadal-scale changes in temperature, precipitation (Girs 1971b), and rotation of the solid Earth (Sidorenko and Svirenko 1988, 1991).

Similarly, an index representing decadal-scale anomaly trends of large-scale atmospheric circulation over the North Pacific Ocean and North American continent is known as the Pacific Circulation Index (PCI: King et al. 1998). As with ACI, PCI reflects the dominant direction – zonal versus meridional - of large-scale wind patterns. PCI is derived in much the same way as ACI. Information is gleaned from analysis of daily sea-surface-pressure fields over the North Pacific and North American region and used to construct synoptic maps whose 'topography' is used to classify atmospheric circulation patterns according to the Girs (1971) classification scheme. Winter-month averages are computed, anomalies generated, and cumulative sums calculated. The PCI record is available for the full 20th century.

King et al. (1998) compared PCI to the time-integral of the Aleutian Low Pressure Index (csALPI). Strong correspondence exists between their records of variability, despite the fact that the two indices are derived using different metrics (see WKT table 1). They conclude that the winter PCI provides a single-index representation of the multiple influences and sub-processes associated with anomaly trends of ALPI. In a similar manner, we use both ACI and PCI to gain insight into cumulative forcings of wind-flow patterns and their associated sub-processes on dynamics within the stadium wave.

Proxy indices: Motivated by observations of secular-scale variability in a variety of proxy indices and by their apparent relationships to either temperature or sub-processes within the stadium-wave network, we have added several proxies to our expanded index collection. The proxy indices used here include:

i) An 825-year sub-decadally resolved (annual resolution available for the portion used in this study) record of *Globigerina bulloides* abundance, available through 2009 (GB: Black et al. 1999; personal communication), as measured from marine sediment in the Cariaco Basin off the coast of Venezuela – a proxy associated with latitudinal migrations of the Atlantic mean Intertropical Convergence Zone (ITCZ).

ii) Monthly resolved records of Sr/Ca isotope ratios in corals from Palmyra Island (Nurhati et al. 2011) that capture a century-long record of sea-surface-temperatures (SST) of the central Pacific tropics (162ºW, 6ºN) - a region that on decadal time scales is linked with extratropical climate variability related to the North Pacific Gyre Oscillation (NPGO: Di Lorenzo et al. 2008). The NPGO affects dynamics of the Kuroshio-Oyashio western-boundary-current and its extension, the North Pacific Current (Ceballos et al. 2009; Di Lorenzo et al. 2010).

iii) Japanese Sardines (JS: Klyashtorin 1998; Noto and Yasuda 1999, 2003), whose population outbursts off the Japanese coast are spatially related to the meridional migrations of the western-boundary current (Kuroshio Current) and its extension (Oyashio Front) and temporally associated with positive polarities of Pacific ocean-atmospheric circulation patterns (PDO, NPO, NINO, ALPI). Annually resolved commercial statistics are available since 1920. Japanese chronicles extend the record to 1640 (Kawasaki 1994).

iv) Earth's rotational-rate anomalies, whose fluctuations have been systematically documented via telescope since ~1623 and are measured in terms of the negative length-of-day index (ngLOD: Stephenson and Morrison 1984), represent the difference between an actual (astronomical) day and the mean length-of-day (86,400 seconds). Rotational-rate anomalies, measured in milliseconds (ms), are physically linked to a variety of geophysical processes, their associated impacts on Earth's axial angular momentum and moment of inertia invoked to rationalize observed correlations (Lambeck and Cazenave 1976; Dickey et al. 2011). At high-frequency timescales, with variations of ~0.2 to 0.4 ms, atmospheric circulation accounts for the majority of ngLOD variability (Dickey et al. 2007). At low-frequency timescales, with multidecadal variations of 4 to 8 ms, atmospheric circulation and related sub-processes of precipitation and global redistribution of water account for ~14% of the magnitude of ngLOD variability (Gross 2005); the remainder attributed to interactions within the Earth's interior (Jault et al. 1988), suggesting a mechanism common to both factors (Sidorenkov et al. 2005; Sidorenkov 2005, 2009; Dickey and Marcus 2011).

Dickey and Marcus investigated a hypothesized relationship between ngLOD and the global surface average temperature in their 2011 paper (hereafter DM; 2011). Examination of a 140-year record of observed and modeled temperature data revealed strong correlation between the two indices until the 1930s, after which the surface temperature trend increased much more than that of ngLOD. DM removed the estimated anthropogenic footprint from the surface average temperature to generate a 'corrected' temperature, one assumed to reflect only natural variability. Correlation between ngLOD and the 'corrected' temperature was strong.

We use annually resolved ngLOD as a proxy for patterns of long-period variability in large-scale wind flow, which are related to the multidecadal components of surface average temperatures, in particular, Arctic temperature (Klyashtorin et al. 1998).

v) The Atlantic SST Dipole (Dipole: Latif et al. (2006); Keenlyside et al. (2008)) is based on sea-surface-temperatures (**SST**: Rayner et al. 2003; 2006[3]) between mid-latitudes of the North and South Atlantic Oceans. The Dipole index isolates SST variability related to variations in the Atlantic sector of the meridionally overturning circulation (AMOC). We use the Dipole as a proxy for meridional migrations of the ITCZ, which studies suggest is 'pushed' northward (southward) with intensification (weakening) of the AMOC, the consequent atmospheric heat transports effectively compensating for the northerly directed, cross-equatorial ocean heat

[3] Rayner et al. 2003 record 1871-2000; Rayner et al. 2006 record 1850-2004.

transport related to dynamics of the AMOC (Zhang and Delworth 2005; Kang et al. 2008; Frierson and Hwang 2012; Donohoe et al. 2013; Marshall et al. 2013).

Note: indices plotted in their negative polarity are indicated by the prefix, ‘ng’. The prefix is chosen over the negative sign as it is easier to see on charts and figure legends. If the index has no prefix, it represents positive polarity.

2.2 Methods

Prior to analysis, all raw indices were linearly detrended (least squares method), resulting in a mean of zero. Our intent in removing the linear trend was to remove the centennial scale trend to highlight multidecadal variability. After the data are linearly detrended, the values are normalized to unit variance, thereby facilitating intercomparison of index behavior.

The cornerstone of our analysis is the Multichannel Singular Spectrum Analysis (M-SSA: Broomhead and King 1986; Elsner and Tsonis 1996; Ghil et al. 2002). M-SSA is used to extract and characterize dominant spatio-temporal patterns of variability shared by indices within a network. The technique is particularly skillful in identifying signals from relatively short, noisy data sets and in identifying non-zero-lag, or propagating, relationships (Ghil et al. 2002). Both high-frequency oscillatory signals and secularly varying trends can be extracted using M-SSA. Mean values of these M-SSA-extracted patterns, or modes of index co-variability, are plotted on an M-SSA spectrum and error bars (based on North et al. 1982 criterion) appended.

To estimate the error bars, the variance of the mode is multiplied by the square root of $2/N^*$, where N^* = the number of degrees of freedom. $N^*=N(1-r^2)/(1+r^2)$, where N is the length of each time series in the index set. One-hundred-year time series for each index were auto-correlated. The auto-correlation plots showed that the maximum autocorrelation after one year among the eight indices was r~0.65. Using this auto-correlation value in the Bretherton formula (Bretherton et al. 1999), the effective number of degrees of freedom was estimated to be 40. From this, the projected decorrelation time is N/N^* = 100/40 = 2.5 years. This is considered the amount of time after which each data point can be considered independent from the ones preceding and following it.

In the original stadium-wave study (WKT), M-SSA extracted two leading modes of variability. Together, the two leading modes captured the complex spatial and temporal characteristics of a secularly varying, hemispherically propagating signal. The likelihood that a low-frequency signal, characterized by a delayed alignment of spatially and dynamically diverse indices, i.e. a hemispherically propagating signal, could be due to mere random chance was found to be less than 5%. This is the signal we further explore through the expanded database.

There is a risk of adding too many indices when applying M-SSA, which can lead to overfitting, distorting the results. Additional spatial information must be introduced to avoid this caveat. We do this by appending regions heretofore unexplored: e.g. the Arctic and tropical Atlantic latitudes. We evaluate numerous subsets of the expanded data base, network sizes ranging from four to 20 members, all combinations hemispherically representative.

To visualize this signal as it is expressed in each index, M-SSA modes are represented in their original index space by reconstructed components (RCs). A reconstructed component is effectively the narrow-band filtered version of an original index time series. RCs of the identified leading modes, summed and normalized, generate the stadium-wave filter for index networks.

A second method applied to our raw-data sets, and done independently from the M-SSA exercise, is correlation analysis. Correlated indices, considered along with M-SSA results, potentially add further insight into dynamics associated with the signal's propagation. Prior to computing correlations between pairs of linearly detrended, normalized raw time series, values were smoothed with a 13-year running mean filter to sort out shorter-term fluctuations in order to highlight longer-term behavior of indices. We also experimented with a variety of filter sizes, from five years to 20; results were virtually unchanged.

We also introduce transformed time series to convey insight into forcings and responses among indices whose behaviors are interconnected within a network. Transformed time series include two types: time-integrated, such as ACI and PCI, and time-differentiated values. The former yields anomaly trends of an index's time series; while the latter converts time series of indices into incremental values – an approximation of the time-derivative of a trend (e.g. AT is the approximate time-derivative of ACI). Transformed indices are useful in detecting potential cause-and-effect relationships. We focus on the time-integrated transformation in this study.

To transform a raw time series into its anomaly trend, or time integral (Hurst 1951; Outcalt et al. 1997), one computes a cumulative sum from a time series of anomalies (raw time series linearly detrended via least-squares method and normalized to unit variance). Cumulative sum (cs) of a time series of anomalies, X, is obtained via equation (1):

$$X(cs)_{(n)} = X_{(n)} + Xcs_{(n-1)} \qquad (1)$$

where $X(cs)_{(n)}$ is the cumulative-sum value at time n; $X_{(n)}$ is the anomaly time-series value at time n; and $X(cs)_{(n-1)}$ is the cumulative-sum value at n-1.

We use a red-noise model to test the statistical significance of spatial and propagation properties of the M-SSA-identified low-frequency signal and also of the correlation analysis results. The red-noise model, used to generate surrogate time series, is fitted independently to each index time series of raw values previously detrended and normalized and has the form:

$$x^{n+1} = ax^{n} + \sigma w, \qquad (2)$$

where x^n is the simulated value of a given index at time n; x^{n+1} is its value at time $n+1$; w is a random number drawn from the standard normal distribution with zero mean and unit variance, while parameters a and σ are computed by linear regression.

Resulting surrogate time series are subject to the same analyses, M-SSA and correlation analysis, as are the 'real data' time series. Analyses on the surrogate values are repeated 1000 times and the 95th percentile of results is computed (see WKT and WP for details).

3 Stadium-wave relationships

The stadium-wave signal propagation sequence through the network of eight original indices is shown in **Figure 2a**. Low-frequency behavior is evident, although the random occurrence of a multidecadal tempo in a time series of only 100 years cannot be ruled out. WKT therefore did not assign an exact period to the signal; rather, the signal is described as secularly varying, with an apparent 64-year period during the 20th century. Despite limitations of a short time series, its short length does not prevent assigning strong statistical significance to patterns of variability that are shared by *all* indices in the network. Regional diversity of indices made this finding more significant, adding a spatial signature to the signal. Phasing-offsets among the indices, repeating in an orderly fashion, indicate the signal's propagating nature. Figure 2**b** shows the leading two modes of the WKT signal plotted on an M-SSA spectrum; $p < 5\%$.

Figure 3 shows a plot of normalized reconstructed components of the stadium-wave signal in one of the 20th-century expanded networks analyzed. In **Figure 4**, mean variances of the modes are plotted on an M-SSA spectrum including error bars and the red-noise envelope. The leading two modes are well-separated from all others, with overlapping error bars, reflecting similar variances of the two modes. This statistically significant signal ($p < 5\%$) is essentially the same signal identified in WKT and was repeatedly identified in other hemispherically representative index combinations, ranging in network size from four members to 20.

The spatially expanded networks reveal dynamical links not apparent in WKT. In addition to the role of the Atlantic Ocean identified by WKT, our results elucidate roles played by the atmosphere and Arctic sea ice. As this signal propagates, distinct regimes of warming or cooling hemispheric temperature trends prevail. Based on this analysis, we propose that there are four stages of a climate regime, which are indicated in the annotation of Figure 3. Each stage is dominated by a particular type of behavior, with a particular geographical focus. Each stage features a subset of indices within the broader network whose behaviors reach peaks and valleys at similar times. We term these four co-varying index clusters 'Temporal Groups' (I-IV).

Not all indices express the signal equally. The amount of variability due to the stadium-wave signal in each index is captured in a channel fraction variance plot (**Figure 5**). The circled regions indicate channel fraction variance values for index clusters of the four Temporal Groups. Indices in Groups I and IV express the signal strongly. Expression of the signal is less in Group II indices. Group III indices have a large range of fractional variances. Channel fraction variance is tied to an index's dominant time scale of variability. Indices with long 'memories' (persistence), which fluctuate at low-frequency tempos, manifest the stadium-wave signal the most strongly. These indices tend to integrate into their 'memory' incremental direct or indirect forcings of higher frequency indices, such as incremental changes in wind or ice cover. We suggest that long-memory indices in Groups I and IV tend to represent the 'cumulative' effect of interacting processes related to higher frequency dynamics. AMO is an example of an index that integrates incremental forcings of higher frequency sub-processes. We will show that it is the long-memory indices that set the signal tempo, while the higher frequency atmospheric indices carry the signal hemispherically and reinforce the low frequency tempo via accumulated sub-process-related forcings incorporated into the ocean memory. Sea ice appears to link the lower and higher frequency indices.

Maximum values of indices characterizing Groups I, II, III, and IV represent the timing of trend reversals of Group clusters as the wave propagates through the four stages of a warming climate regime. Similarly, minimum values of these Group indices represent the timing of oppositely signed trend reversals that occur in sequence as a cooling regime unfolds. In the discussion to follow, we focus on evolution of a warming regime, but it is implicit that a cooling regime evolves similarly but with opposite sign[4].

3.1 Temporal Groups

A Temporal Group's indices tend to reflect a dominant geographic region exhibiting a dominant set of sub-processes. This is especially apparent in Groups I through III. Group IV differs slightly. Instead of representing specific sub-processes of a region, Group IV indices reflect a culmination of influences of anomalies of sub-processes.

Peak activity within each of the four Groups represents stages of climate regime development as the signal propagates through the network. To obtain plots of these Groups, reconstructed components (RCs) of indices whose peak values represent each stage of regime development are extracted from an expanded network (e.g. Figure 3) to which M-SSA was applied. Representative RCs then are plotted according to Group. Tables **3** through **6** reflect correlation values between raw time series (detrended, normalized, and smoothed with a 13-year filter) of index pairs. Significance levels = p<5% are shown in blue; p<1% are shown in red.

[4] Terminology: We refer to Stages of a cooling either as the minima of Groups I through IV, or as peak values of Groups –I, -II, -III, and –IV.

3.1.1 Temporal Group I: Ocean-ice interactions in the North Atlantic sector of the Arctic predominate in this Group. Cool Atlantic sea-surface temperatures (ngAMO) correlate strongly with positive sea ice extent of the Greenland and Barents Seas (NEB) - and by extension, with sea ice of the West Eurasian Arctic (WIE) (Table 3**a**).

Negative PCI co-varies with Group I (Table 3**b**), which may reflect the remote and cumulative teleconnected influence of Pacific circulations on the Atlantic's freshwater balance. An atmospheric bridge, of sorts, conveys Pacific influence on Atlantic precipitation patterns. Through modified atmospheric patterns, associated Pacific sea-surface-temperature anomalies are linked to surface salinity anomalies of the Atlantic, ultimately providing negative feedback to the Atlantic Meridional Overturning Circulation (AMOC) (Latif et al. 2000; Schmittner et al. 2000; Latif et al. 2001), and by extension, the AMO (Knight et al. 2005; Latif et al. 2006; Msadek et al. 2010a), setting the stage for the AMO's subsequent influence on ice inventory. Plotted raw indices in **Figure 6** reflect the relationships among ngAMO, the negatively signed cumulative sum of PDO, and ngPCI – an index related to decadal-scale trends of Pacific circulation patterns.

Globigerina *bulloides* and the Atlantic SST Dipole correlate strongly with Group I indices. Positive values of G. *bulloides* suggest enhanced upwelling of cold water off the coast of Venezuela (Black et al. 1999), which may be associated with a southward displacement of the Atlantic sector of the Intertropical Convergence Zone (ITCZ). The negative polarity of the Atlantic SST Dipole suggests the same. A south shifted ITCZ is linked to a weakened Atlantic meridional overturning circulation (AMOC) (Latif et al. 2006; Donohoe et al. 2013, Kang et al. 2012; Marshall et al. 2013). These dynamics co-occur with the shifting Arctic Front in response to the migrating sea-ice edge (e.g. Zakharov 1997, 2013), related to phase of AMO. **Figure 7** and Table 3**c** reflect these relationships: as sea ice increases with a cool AMO and a weak AMOC, the sea ice edge advances equatorward, and the ITCZ shifts southward (section 2.1), as indicated by positive anomaly values of GB and ngDipole. (See WKT on AMOC-AMO link.) Peaks of index plots occur near ~1918 and 1976, with a minimum at ~1942. These are timings of previously identified climate-regime shifts (Tsonis et al. 2007; Van Loon et al. 2007).

3.1.2 Temporal Group II: Atmospheric response to an ice-induced polar-equatorial meridional temperature gradient, particularly pronounced in the Siberian sector of the Eurasian Arctic, characterizes Temporal Group II (**Figure 8**). Indices peak ~1923 and ~1982 and minimum values center on ~1950. Co-varying indices in Group II include the ice index of ArcSib north of Siberia and AT, a measure of the zonal component of large-scale wind flow. The SST-based proxy representing NPGO also co-varies with this Group. NPGO is a wind-driven ocean-gyre index in the North Pacific, related to both extratropical atmospheric dynamics and to meridional migrations of the Pacific ITCZ. Positive co-variance among these sea ice and wind related indices (**Table 4**) is consistent with a basin-scale wind response to the polar-equatorial meridional temperature gradient (Honda et al. 2009; Petoukhov and Semenov 2010; Outten and Esau 2011): increased sea ice extent inhibits ocean-heat flux to the atmosphere, thus cooling Arctic temperatures, augmenting a meridional atmospheric temperature gradient, and thereby intensifying large-scale wind flow with an enhanced zonal component. Boreal winter indices, NAO and AO[5], also co-vary with Group II.

[5] Winter indices of NAO and AO behave differently from their annual counterparts. In table and figure legends used in this paper, we emphasize the use of winter indices by adding the letter ‘w’: e.g. NAOw and AOw.

3.1.3 Temporal Group III: North Pacific activity and ice-influenced atmospheric dynamics dominate Temporal Group III (**Figure 9**). Continued sea ice attrition west of the Pacific sector and the subsequent increase of ocean-heat flux to the atmosphere in that region remotely influence Pacific circulations by shifting air mass away from the high latitudes, displacing it to mid-latitudes. Latitudinal redistribution of atmospheric mass weakens the Arctic High, effects of which extend to the Pacific as the anomalous low-pressure system expands (e.g. Overland et al. 1999; van Loon et al. 2007), intensifying the Aleutian Low. These processes are reflected in the strong connections between the Pacific centered circulations (NPO, ALPI, and PDO) and *anomaly* trends (cumulative-sums (cs)) of WIE, TIE, and Kara Sea ice (Table 5**a**). We hypothesize that these relationships reflect the incremental influence of sea ice extent fluctuations on the atmosphere that are consistent with observed dynamics (e.g. Zakharov 1997; Bengtsson 2004; Frolov et al. 2009): incremental reductions in ice cover (particularly in the Atlantic sector) lead to increased ocean-heat flux to atmosphere, promoting a decrease in sea-level-pressure of the Arctic High, the influence of which ultimately extends into the Pacific (e.g. Overland et al. 1999; van Loon et al. 2007). Group III indices peak ~1929-1933 and ~1985-1990.

The multidecadal component of EIE – sea ice of the Laptev, East Siberian, and Chukchi Seas – positively co-varies with Pacific centered circulations. The sea ice edge in the Pacific shifts southward with increasing trends in this stage (Asmus et al. 2005; see Frolov et al. 2009), coinciding with a weakening Arctic High, displacement of atmospheric mass equatorward, and an increased number of cyclones co-varying with an intensified Aleutian Low.

Centuries-long records reveal decadal-scale variability of Japanese sardine outbursts in the Kuroshio-Oyashio western-boundary-current extension. Japanese sardine outbursts co-vary positively with Pacific circulations - PDO, in particular (Table 5**b**). Fueling these outbursts is an increased supply of nutrients – a product of a deepened mixed-layer depth (Polovina et al. 1995). Yasuda (2003) demonstrate a relationship between Japanese sardine outbursts and a deepened mixed-layer-depth to 'Oyashio Intrusions' - southward shifts of the Kuroshio-Oyashio boundary – the ocean-gyre boundary that separates the Oyashio Current of the subpolar region from the Kuroshio Current of the subtropical zone. The Kuroshio-Oyashio front shifts southward as the sea ice edge in the Pacific sector of the Arctic advances and as PDO increases (Miller and Schneider 2000). Between the mid-1960s to the mid-late 1980s EIE and Pacific circulations increased. Japanese sardine populations also increased. The mixed-layer depth was unusually deep (Yasuda et al. 2000). Similar trends occurred between ~ 1905 and the early 1930s as Group III indices were increasing.

***3.1.4 Temporal Group IV*:** High latitudes of the Northern Hemisphere are the focus in Temporal Group IV. The culmination of anomaly trends of the various large-scale wind and wind-related patterns, particularly those related to Group II, are featured (**Figure 10**). They co-vary with the Arctic temperature and NHT, perhaps indicating a relationship between intervals of anomalies (in sea ice extent, corresponding ocean-heat flux, and associated winds and wind-related dynamics) and the overlying temperature. Correlations among these indices are listed in Table 6**a** and further discussed in section 4. The anomaly trend of ArcSib leads indices of this Group by ~3 years. Also co-varying with this Group is Earth's rotational rate (ngLOD). It is strongly correlated to the anomaly trend of large-scale wind patterns (csAT) and by extension, the Arctic temperature and NHT (section 2.1 and Table 6**b**).

Maxima of Group IV indices occur around 1938 and 1998. At these times of peak Arctic temperature and NHT, AMO is nearing maximum warmth, sea ice in NEB and WIE continues to shrink (Table 6**c**), and the poleward retreated sea ice edge in the Atlantic sector displaces the Arctic Front far northward. The Atlantic ITCZ is similarly displaced. Minima center on ~1910 and 1971 and host the same dynamics, yet of opposite sign.

3.2 Changing Index Relationships as a Regime Evolves

Index relationships appear complex as the regimes evolve. **Figure 11** simplifies the pattern: trends of successive Group-indices systematically and sequentially reverse as the signal propagates through stages of a regime. Stages, which coincide with peaks of each Group, are indicated by vertical lines. Each Temporal Group is represented by one index (e.g. AMO, AT, PDO, and Arctic T) for the sake of simplicity, and all indices are shown as *positively* signed[6] in order to illustrate our point. Ice indices are *not* included in this discussion; only ocean, atmosphere, and temperature indices are considered. The chart begins in 1910 (peak of Group – IV) with a transition from a cooling regime to a warming one. In ~ 1910, prior to the beginning of the warming regime that began ~1918, indices representing Groups II through IV are trending together (red lines). Their values are increasing, while AMO of Group I is trending out-of-phase (blue line). An AMO trend in opposition to other indices marks the transition between regimes.

Once the AMO reverses trend, as it did in ~1918 at the peak of Group I when the Atlantic was at its coolest, all indices of *all* Groups are increasing. This shared uni-directional upward trend among indices distinguishes an incipient warm regime – i.e. stage I. As the wave progresses through the network sequence, passing through successive stages, indices begin to reverse trend direction, one-by-one.

After the peak of Group II, all indices continue to increase except for AT and its co-varying Group II indices. After the peak of Group III, AT and PDO, and related indices have

[6] This is in contrast to AMO in all stadium-wave figures, where AMO is plotted in its negative polarity (ngAMO).

reversed trend, now decreasing. AMO and surface temperatures continue an upward trend until the peak of Group IV. After the peak of Group IV, AT, PDO, and ArcT are all decreasing; while only AMO continues to increase. This continued upward trend of AMO, co-occurring with all other indices in decline, marks the transition at the end of the warming regime, leading into a cooling regime. After a several year transitional interval, the ensuing cooling regime begins with AMO reversing trend ~ 1942. All indices decrease during this initial stage of a cooling regime. Stages one through four of the cooling regime, indicated by peaks of Groups –I through –IV, lead to the next regime transition in ~1971. A new regime of warming begins ~1976.

4 Stadium-Wave Mechanisms

WKT hypothesized that the stadium-wave signal propagates through a hemispheric network of synchronized climate indices. We have argued that through this propagation, climate regimes evolve in four stages. Low-frequency variability of sea ice extent in the Eurasian Arctic Seas is a critical component underpinning the hypothesized signal and multi-decadal scale evolution of climate regimes.

What makes sea ice in this particular region so fundamental to the wave's existence? Sea ice in the Northern Hemisphere is uniquely exposed to open ocean (the North Atlantic) in the Eurasian Arctic. This juxtaposition governs sea ice growth by giving the Atlantic Ocean dominant constructive or destructive influence over the feature mostly responsible for wintertime sea ice cover, the halocline. The halocline is a subsurface zone, approximately 150 meters thick, where salinity concentration changes rapidly with depth; in the North Atlantic sector of the Arctic, salinity values decrease with depth. Formation of the halocline relies upon the interaction between layers of water with contrasting properties: Overlying cool, desalinated Arctic surface water mixes with warm, saline water below. The halocline's resulting vertical density structure, in turn, maintains separation between the two water masses and prevents ocean heat at depth from reaching the surface. Where a strong halocline exists, sea ice growth is promoted (Zakharov 1997; Frolov et al. 2009 and references within). Ice extent influences large-scale wind patterns, which influence long-term temperature trends (e.g. Outten and Esau 2011). Thus dynamics that either build or destroy the halocline in the North Atlantic sector of the Arctic have a marked influence on climate-regime evolution as the stadium-wave propagates through the network.

The schematic of **Figure 12** and sections 4.1 through 4.5 summarize the stadium-wave's propagation through the four stages of climate regime evolution. We discuss only stages I through IV of the evolution of a warming regime. (Stages –I through –IV of the cooling regime are simply opposite.)

4.1 Processes and Trends Relate to Stage I

A regime of warming temperature commences with maximum cool sea-surface temperatures in the North Atlantic. Sea ice extent in the West Eurasian Arctic (WIE) is at maximum values. ITCZ is displaced to its most southerly position. For a decade-plus *prior* to these index maxima, conditions conducive to sea ice growth in the Atlantic sector of the Arctic have been building. These include high sea-level-pressure anomalies in the Arctic High. Associated with the high sea-level-pressure anomalies are anticyclonic-wind anomalies that govern sea ice export patterns within the WIE region. Their net effect is to bolster halocline development through freshening of the Greenland, Barents, and Kara Seas (Bengtsson et al. 2004; Frolov et al. 2009 and references within). The atmospheric Arctic Front shifts southward with the advancing ice edge (Zakharov 1997). Precipitation zones shift southward, gradually reducing freshwater delivery to the Arctic –

a negative feedback sowing future reversal of the regime against a backdrop of dominantly positive feedbacks reinforcing sea ice growth. This stage ends with AMO, WIE, and ITCZ having reversed their trends.

4.2 Processes and Trends Related to Stage II

Sea ice of WIE dominates, despite its recently reversed trend. Even though AMO is slowly warming, ocean heat flux is inhibited by the ice cover and the atmosphere at high latitudes chills. Simultaneously, yet in quadrature offset, EIE in the Laptev, East Siberian, and Chukchi Seas is growing. Group II indices respond to the increasing, albeit eastward shifting, distributions of total ice cover – a region dominated by the Kara Sea. Total ice cover, specifically ArcSib, co-varies with a strong meridional temperature gradient that simultaneously develops between the ice and snow covered surfaces of high latitudes and the warm surfaces of lower latitudes in the Eurasian region. In atmospheric response, large-scale winds (AT) strengthen; their zonal component advecting heat and moisture from the lower latitudes of the Atlantic Ocean to the mid-to-high latitudes of the Eurasian landmass downwind, disrupting previously stable surface conditions and increasing high cloudiness, both changes leading to increasing continental temperatures, in particular those at low altitudes and higher latitudes (e.g. Van Loon et al. 2007). Cyclonic (negative sea-level-pressure) anomalies weaken the Arctic High; westerly winds increase in intensity, further advecting atmospheric heat and moisture eastward. WIE from Group I is now decreasing, in part due to changing sea ice export patterns. The cyclonic winds altering the ice export pattern that previously augmented the WIE inventory now are restricting the freshwater supply to the western marginal seas (Gudkovich and Nikolayeva 1963; see Frolov et al. 2009). The Arctic Front's southward displacement continues to deprive the Arctic of precipitation and related runoff. The anomalous cyclonic winds dynamically impact the ice, leading to open cracks in the ice surface through which heat from the ocean escapes, heating the overlying atmosphere. Winds increase influx of warm Atlantic water into the Arctic. The initial cold signal converts to a warming one. Initially, ice scripted the atmospheric response. The atmosphere now begins directly and indirectly to modify the ice cover. The Atlantic sea ice edge retreats, its progress traced by similar northward migrations of the Arctic Front and the ITCZ. Ocean-heat flux to the atmosphere increases. Surface temperatures increase. The regime thus far built by processes reflecting the stadium-wave propagation through Group I and II indices continues to mature. The halocline is now deteriorating, inhibiting sea ice growth. ArcSib has reached peak values and WIE is in decline.

4.3 Processes and Trends Related to Stage III

As the ArcSib and resulting winds related to AT and NPGO begin to wane, WIE continues to decrease and AMO continues to warm along with surface air temperatures. Westerlies continue to dominate, albeit more shifted toward the North Pacific. Atmospheric (NPO, ALPI) and related oceanic patterns (PDO) are increasing as an indirect result of the sea ice attrition in WIE. Enhanced ocean-heat flux leads to lower SLP anomalies in the Arctic High. The deepened center-of-action extends well into the North Pacific, intensifying the Aleutian Low, which shifts its center south and east. East Eurasian sea-ice (EIE) governed by complex and competing ice-atmosphere-ocean interactions, increases with strengthening Pacific circulations, tracking in-quadrature with AMO and WIE. Wind-flow patterns in the Atlantic sector of the Arctic are decreasing the freshness of the shelf seas in the western Eurasian region, via modified sea ice export patterns between the Arctic Basin and marginal seas (Subbotin 1988; Frolov et al. 2009).

This overarching process coincides with a second, more localized wind pattern that is generated by a sea-level-pressure anomaly, the source of which lies near the Barents-Kara border. These winds, confined to the lower troposphere, now coax an influx of saline water from the warming Atlantic into the Barents and Kara Seas (Bengtsson et al. 2004). Both wind-related patterns reduce the halocline. WIE continues to diminish and ArcSib is in decline. As the signal continues its propagation, this penultimate stage of climate-regime development begins to weaken and all of sea ice indices now are decreasing: WIE, ArcSib, TIE, and EIE. The sea ice edge in the western Eurasian Arctic continues its poleward retreat.

4.4 Processes and Trends Related to Stage IV

By the time Group IV indices begin to peak, positive anomalies of ArcSib and its associated winds cease. The Arctic temperature and NHT reach maximum values. Unlike at other stages of regime development, no sub-processes of our expanded network peak at stage IV. Instead, anomaly trends peak, representing the conclusion of a multidecadal stretch of anomalies of sub-processes related to Group II. These anomaly trends represent the *culmination* of impacts related to interlinked changes in sea ice extent, ocean-heat flux, sea-level-pressure, large-scale wind and sea-ice-export patterns, position of Arctic Front, and consequent atmospheric heat and moisture influx into the Arctic (Zakharov 1997; Francis and Hunter 2007) - their collective interaction coinciding with an increased influx of Atlantic Intermediate Water into the Arctic, the temperature anomalies of which closely co-vary with Arctic temperatures (Bengtsson et al. 2004; Polyakov et al. 2004, 2005, 2010). In effect, incremental forcings resulting from a cascade of feedbacks reducing sea ice extent appear to be integrated into the system. The product of their collective impact is expressed in peak values of Arc T. NHT lags by about a year or two.

Simultaneous with the culmination of anomalies that have been collectively destroying ice and delivering heat to the Arctic are processes that counter this trend. One example is the poleward displacement of the Arctic Front due to the retreating sea ice edge. Precipitation and associated runoff are similarly displaced poleward. They are major supplies of freshwater for the subsequent regime's ice growth. But for now, only decreasing ice, increasing Atlantic sea-surface temperatures, and warming surface-air temperatures are apparent.

4.5 Transition: After temperatures peak, surface temperatures begin to decrease, while AMO continues to warm and sea-ice extent continues to wane. This short duration of seemingly incongruent index trends marks regime transition, indicated by dashed line on Figure 12, from the peak of Group IV to the regime reversal at the peak of Group –I. Once the peak of Group –I is reached, a maximally warm AMO reverses trend; WIE begins to rebound. A new regime of cooling begins - punctuation on a continuum of an ever evolving, quasi-oscillatory system.

5 Summary and Discussion

We used multivariate statistical analysis to extend the WKT hypothesis of a secularly varying signal hemispherically propagating through a network of synchronized climate indices during the 20th century. We expanded the original database with the incorporation of Arctic sea ice and a variety of other parameters, including proxy data reflecting sub-processes within the wave. Sea ice in the shelf seas of the Eurasian Arctic region emerged in this study as playing the pivotal role in propagating and sustaining the 20th century stadium-wave signal, with interaction of positive and negative feedbacks governing the ice coverage and related atmospheric/oceanic responses.

We found that the stadium-wave signal propagates through four different stages of climate regime evolution. Each stage reflects a particular behavior or a particular set of sub-process interactions. And at each stage, activity is heightened in a particular geographic region. At all stages, seeds of regime reversal are embedded within the collection of sub-processes regulating the Arctic freshwater balance, thereby subtly and incrementally imposing 'curbs' on the prevailing trend of sea ice coverage, assuring an inevitable regime reversal years in the future. These negative feedbacks modify the Arctic freshwater balance through: i) sea ice related shifts in the Arctic Front and associated zones of precipitation and continental runoff; ii) ice-cover associated sea-level-pressure changes that reorganize winds and thereby direction of freshwater and sea ice export between the Arctic Basin and marginal seas; iii) modified influx of warm, saline water into the marginal seas, particularly in the Atlantic sector; iv) and Pacific atmospheric circulation anomalies negatively feeding back onto the Atlantic freshwater balance through remote modification of precipitation regimes.

A robust halocline and extensive ice cover introduce a warm regime and promote processes that lead to their destruction. Overshadowed are the accruing embedded 'curbs' that ultimately moderate the destruction and bring a warm regime to its close. Reduced ice cover and a weak halocline at the end of a warming interval initiate a cooling regime whose dynamics collectively rebuild the halocline and ice cover, accompanied by an accumulating influence of embedded 'curbs' that ultimately reverse the trend. Our results for this multidecadal component of Eurasian Arctic dynamics are consistent with the ideas of Zakharov (1997) who describes the oscillatory nature of the ice-ocean-atmosphere system in terms of 'braking' – the idea that positive and negative feedbacks interact in such a way as to limit trends of sea ice growth and sea ice destruction.

Sub-processes that interact to impose this blueprint of positive and negative feedbacks and the consequent temperature trends are schematically summarized in **Figure 13**. This stadium-wave 'wheel' cartoon representation combines components involved in stadium-wave propagation with the co-varying proxy indices. The wheel is divided into eight segments, each representing a Temporal Group of co-varying indices: four positive-polarity Groups and four negative-polarity Groups. Roman numerals designating the Temporal Group number are positioned at the narrow end of its associated segment. Indices of each Temporal Group populate the designated wheel segment. Dates on the perimeter indicate dates around which the indices peaked (or are projected to peak); these dates represent stages of regime development: four stages for a warming regime (dates in red) supplanted by four stages of a cooling regime (dates in blue). Differently colored rings host indices belonging to shared process or medium, e.g. WKT indices in the inner grey ring; ice indices in the yellow ring; wind related ones in the blue; and co-varying proxy indices in the outer green ring. Read clockwise to follow the propagating wave as it moves through each of the three systems – ocean, ice, and wind – divided among the Temporal Groups, the peaks of which represent stages of climate-regime evolution, the processes of which leave traces etched into the co-varying proxy indices.

By framing regime evolution in context of stadium-wave propagation, we gain insight into behaviors resulting from the temporal alignment of the different stages. For example, McCabe et al. (2004) document drought patterns of the western United States, finding their occurrences increase with warm AMO phases. North-south distribution of drought patterns is further scripted by which phase of PDO co-occurs with AMO. The stadium wave also provides perspective on seemingly discordant observations. Examples can be found in the previously discussed out-of-phase alignment of surface air temperature with AMO that occur during hypothesized transitions between regimes; and in changing trends of sea ice among the various seas during intervals of dominantly positive or negative surface temperature anomalies.

We suggest that the stadium-wave hypothesis holds promise in putting in perspective the numerous observations of climate behavior; offers potential attribution and predictive capacity; and that through use of its associated proxies, may facilitate investigation of past behavior that may better inform our view of future behavior.

In recent decades, rapid changes in the Arctic have been documented (e.g. Alkire et al. 2007). Most interpretations of the recent decline in Arctic sea ice extent have focused on the role of anthropogenic forcing (e.g. Johannessen et al. 2004), with some allowance for natural variability (e.g. Zhang el al. 2010). How can we interpret the recent decline of Arctic Sea ice extent in context of the stadium wave? Alexeev et al (2013) observe pronounced low ice coverage between 2004 and 2008 and conclude it is primarily linked to the temperature of the influx of the Atlantic Intermediate Water (AIW; Polyakov et al. 2004, 2010) into the Barents Sea. Data values of the Eurasian region in 2008, not included in our analysis, indicate maximum summer ice-cover destruction in the ArcSib region east of the Barents Sea, accompanied by late-onset of sea ice growth the following winter months. And further to the east, influx of warm Pacific water through the Bering Strait has been identified (Shimada et al. 2006; Wang et al. 2009; Alexeev et al. 2013) as one factor contributing to the Arctic sea ice decline there. None of these observations are inconsistent with the stadium wave, which if extrapolated beyond the 20th century, reflects low ice in all three regions cited: the WIE, ArcSib, and EIE (see Figure 3). But according to stadium-wave projections, and according to our interpretation of stadium-wave evolution, this trend should reverse, under the condition that the stadium-wave hypothesis captures 20th century dynamics correctly. Rebound in WIE, followed by ArcSib should occur after the estimated 2006 minimum of WIE and maximum of AMO (e.g. Figures 3, 10, and 13).

Timmermans et al. (2011) measured a notable increase in surface freshening of the region of the Greenland Sea, between the North Pole and the Fram Strait in 2010 that was not due to summer melt. Using models to interpret their observations, they concluded that relatively abrupt changes documented to have occurred in 2009 in large-scale wind patterns could account for freshening via re-distribution of freshwater within the Arctic and an increase in river runoff. Timmermans et al. concede that they cannot speculate on duration of this observed freshening and wind shift, but note that the upper-ocean salinity changes are not of seasonal origin.

While evidence strongly supports our hypothesis of a secularly varying climate signal propagating through a hemispheric network of synchronized ocean, atmosphere, and ice indices during the 20th century, we cannot know if this variability, tempo, and sequential chronology will continue into the future. How changes in external forcing might affect the Eurasian Arctic sea ice in context of an apparent quasi-oscillatory ocean-ice-atmosphere system is a burning question.

Modeled results are often invoked to guide projected climate trends, yet WP found no decadal to multidecadal-scale hemispherically propagating signal in networks of indices simulated from data generated by runs of the CMIP3 suite of models, leading to the inference that 21st-century model simulations may not accurately capture dynamics necessary to reconstruct stadium-wave behavior.

Understanding how stadium-wave behavior might respond to changing external forces may be facilitated by extending the record prior to the 20th century via proxy data. Evaluation of 300-year records of proxies by Wyatt (2012) suggests that changes occurred in tempo and amplitude prior to the 1800s, perhaps in response to changes in external forcing. Proxy-process relationships established throughout the paper, representing the proposed four stages of climate-regime evolution, suggest a means of extending the stadium-wave signal's record, providing potential insight into attribution of behavior past, present, and future.

Acknowledgments We thank S. Kravtsov for helpful guidance on statistical aspects of this study; Vasily M. Smolyanitsky, who provided data and helpful feedback on our work; and two anonymous reviewers for comments on an earlier version of the manuscript, which helped clarify the presentation. Judith Curry's contributions to this paper were supported by a DOE STTR grant.

References

AARI (2007) Sea ice charts of the Russian Arctic in gridded format 1933-2006, Arctic and Antarctic Research Institute, edited by: Smolyanitsky V, Borodachev V, Mahoney A, Fetterer F, Barry R, Boulder, Colorado USA, National Snow and Ice Data Center, Digital media

Alexeev VA, Ivanov VV, Kwok R, Smedsrud LH (2013) North Atlantic warming and declining volume of arctic sea ice. The Cryosphere Discussions 7:245-265 doi:10.5194/tcd-7-245-2013

Alkire MB, Falkner KK, Rigor I, Steele M, Morison J (2007) The return of Pacific waters to the upper layers of the central Arctic Ocean, Deep Sea Research Part I. 54: 1509-1529

Asmus VV, Krovotyntsev VA, Milekhin OE, Trenina IR (2005) Study of Multiyear Dynamics of Sea Ice in the Arctic from Satellite Radar Data: Issues of Processing and Interpretation of the Earth's Radar Sounding Data. St. Petersburg: Gidroeteoizdat [proc. RC Planeta, 1(46): 155-172 [in Russian]]

Beamish RJ, McFarlane GA, Noakes D, King JR, Sweeting RM (1998) Evidence of a new regime starting in 1996 and the relation to Pacific salmon catches (NPAFC Doc 321) 31p. Dept of Fisheries and Oceans, Sciences Branch-Pacific Region, Pacific Biological Station, Nanaimo, BC, Canado V9R 5K6

Bengtsson L, Semenov VA, Johannessen OM (2004) The Early Twentieth-Century Warming in the Arctic – A Possible Mechanism. J Clim 17:4045-4057

Black D, Peterson LC, Overpeck JT, Kaplan A, Evans MN, Kashgarian M (1999) Eight Centuries of North Atlantic Ocean Atmosphere Variability. Science 286: 1709-1713. doi: 10.1126/science.286.5445.1709

Bretherton, C.S, Widmann M, Dymnikov VP, Wallace JM, Blade I (1999) The effective number of spatial degrees of freedom of a time-varying field. J Clim 12: 1990–2009

Broomhead DS, King GP (1986) Extracting qualitative dynamics from experimental data. Physica D 20: 217–236

Ceballos LI, Di Lorenzo E, Hoyos CD, Schneider N, Taguchi B (2009) North Pacific Gyre Oscillation synchronizes climate fluctuations in the eastern and western boundary systems. J Clim 22: 5163-5174

Dickey JO, Marcus SL, Chin TM (2007) Thermal wind forcing and atmospheric angular momentum: Origin of the Earth's delayed response to ENSO. Geophys Res Lett 34: L17803. doi:10.1029/2007GL030846

Dickey JO, Marcus SL, de Viron O (2011) Air Temperature and Anthropogenic Forcing: Insights from the Solid Earth. J Climate 24:569-574. DOI:10.1175/2010JCLI3500.1

Di Lorenzo E, Schneider N, Cobb KM, Franks PJS, Chhak K, Miller AJ, McWilliams JC, Bograd SJ, Arango H, Curchitser E, Powell TM (2008) North Pacific Gyre Oscillation links ocean climate and ecosystem change. Geophys Res Lett 35: L08607. doi:10.1029/2007GL032838

Di Lorenzo E, Cobb KM, Furtado JC, Schneider N, Anderson BT, Bracco A, Alexander MA, Vimont DJ (2010) Central Pacific El Niño and decadal climate change in the North Pacific Ocean. Nature Geosci 3 (11): 762-765. doi10.1038/NGEO984

Donohoe A, Marshall J, Ferreira D, McGee D (2013) The Relationship between ITCZ Location and Cross-Equatorial Atmosphere Heat Transport: From the Seasonal Cycle to the Last Glacial Maximum. J Clim 26: 3597-3618

Elsner JB, Tsonis AA (1996) Singular Spectrum Analysis: A New Tool in Time Series Analysis. Springer, 177 pp

Francis JA, Hunter E (2007) Changing fabric of the arctic blanket. Environ Res Lett 2: 045011. doi:10.1088/1748-9326/2/4/045011

Frierson DMW, Hwang Y -T (2012) Extratopical influence on ITCZ ahifts in slab ocean simulations of global warming. J Clim 25: 720-733

Frolov IE, Gudkovich AM, Karklin BP, Kvalev EG, Smolyanitsky VM (2009) Climate Change in Eurasian Arctic Shelf Seas, Springer-Praxis Books, ISBN 978-3-540-85874-4, 165p

Ghil M, Allen MR, Dettinger MD, Ide K, Kondrashov D, Mann ME, Robertson AW, Saunders A, Tian Y, Varadi F, Yiou P (2002) Advanced spectral methods for climatic time series. Rev Geophys 40(1): 3.1–3.41. doi:10.1029/2000GR000092

Girs AA (1971a) Multiyear oscillations of atmospheric circulation and long-term meteorological forecasts. L. Gidrometeroizdat 480 p. [in Russian]

Girs AA (1971b) Long-term fluctuations of the atmospheric circulation and hydrometeorological forecasts. L., Hydrometeorological monographs, St. Petersburg, Russia. 280p [in Russian]

Gross RS, Fukumori I, and Menemenlis D (2005) Atmospheric and oceanic excitation of length-of-day variations during 1980-2000. J Geophys Res 110: B09405. doi:10.1029/2004JB003565

Gudkovich ZM and Nikolayeva AYa (1963) Ice drift in the Arctic Basin and its relation to sea ice extent of the Arctic Seas. AARI *Proc* 104: 212. [in Russian]

Gudkovich ZM, Karklin VP, Kovalev EG, Smolyanitsky VM, Frolov IE (2008) Variations of sea ice cover and other constituents of the climate system in the Arctic and Antarctic in connection with polar vortex evolution. Problems of the Arctic and Antarctic 78:48-57 [in Russian]

Honda M, Inoue J, Yamane S (2009) Influence of low Arctic sea-ice minima on anomalously cold Eurasian winters. Geophys Res Lett 36: L08707. doi:10.1029/2008GL037079

Hurst HE (1951) Long-Term Storage Capacity of Reservoirs. Transactions of the American Society of Civil Engineers 116: 770-799

Jault D, Gire C, and Le Mouel J-L (1988) Westward drift, core motions and exchanges of angular momentum between core and mantle. Nature 333: 353-356

Johannessen OM, Bengtsson L, Miles MW, Kuzmina SI, Semenov VA, Alekseev GV, Nagurnyi AP, Zakharov VF, Bobylev LP, Pettersson LH, Hasselmann K, Cattle HP (2004) Arctic climate change: observed and modeled temperature and sea-ice variability. Tellus 56A: 328-341

Kang S, Held I, Frierson, D, Zhao M (2008) The response of the ITCZ to extratropical thermal forcing: Idealized slab-ocean experiments with a GCM. J Clim 21: 3521-3532

Kawasaki, T (1994) A decade of the regime shift of small pelagics – from the FAO expert Consultation (1983) to the PICES III(1994). Bull. Japanese Soc. Fish. Oceanogr 58: 321-333

Keenlyside NS, Latif M, Jungclaus J, Kornblueh L, Roeckner E (2008) Advancing decadal-scale climate prediction in the North Atlantic sector. Nature 453: 84-88. doi:10.1038/nature06921

King, JR, Ivanov VV, Kurashov V, Beamish RJ, McFarlane GA (1998) General Circulation of the atmosphere over the North Pacific and its relationship to the Aleutian Low. (NPAFC Doc. No. 318) 18p, Dept. of Fisheries and Oceans, Sciences Branch

Klyashtorin LB (1998) Long-term climate change and main commercial fish production in the Atlantic and Pacific. Fisheries Research (37): 115-125

Klyashtorin LB, Lyubushin AA (2007) Cyclic Climate Changes and Fish Productivity. Moscow, VNIRO Publishing, Editor for English version: Dr. Gary D. Sharp, Center for Climate/Ocean Resources Study, Salinas, CA. USA: 223pp

Knight JR, Allan RJ, Folland CK, Vellinga M, Mann ME (2005) A signature of persistent natural thermohaline circulation cycles in observed climate Geophys Res Lett 32: L20708. doi: 10.1029/2005GRL024233

Kwok R (2011) Observational assessment of Arctic Ocean sea ice motion, export, and thickness in CMIP3 climate simulations. J Geophys Res vol 116 C00D05. doi:10.1029/2011JC))7004

Lambeck K, Cazenave A (1976) Long Term Variations in the Length of Day and Climate Change. Geophysical Journal International 46(3): 555-573

Latif M, Roeckner E, Mikolajewicz U, Voss R (2000) Tropical Stabilization of the Thermohaline Circulation in a Greenhouse Warming Simulation. J Clim 13: 1809-1813

Latif M (2001) Tropical Pacific/Atlantic Ocean Interactions at Multi-Decadal Time Scales. Geophys Res Lett 28: 539-542

Latif M, Böning C, Willebrand J, Biastoch A, Dengg J, Keenlyside N, Schweckendiek U, Madec G (2006) Is the thermohaline circulation changing? J Clim 19 (18): 4631-4637. doi: 10.1175/JCLI3876.1

Marshall J, Donohoe A, Ferreira D, McGee D (2013) The ocean's role in setting the mean position of the atmosphere's ITCZ. Clim Dyn: DOI 10.1007/s00382-013-1767-z

McCabe, Gregory J.; Palecki, Michael A.; Betancourt, Julio L (2004) Pacific and Atlantic Ocean influences on multidecadal drought frequency in the United States. PNAS. 101 (12): 4136-4141. DOI/10.1073/pnas.0306738101

Miller AJ and Schneider N (2000) Interdecadal climate regime dynamics in the North Pacific Ocean: theories, observations and ecosystem impacts. Progressive Oceanography. 47(2-4): 355-379

Msadek R, Dixon KW, Delworth TL, Hurlin W (2010a) Assessing the predictability of the Atlantic meridional overturning circulation and associated fingerprints. Geophys Res Lett 37: L19608. doi: 10.1029/2010GL044517

North GR, Bell TL, Cahalan RF, Moeng FJ (1982) Sampling errors in the estimation of empirical orthogonal functions. Monthly Weather Review 110: 669–706

Noto M, Yasuda I (1999) Population decline of the Japanese sardine, *Sardinops melanostictus*, with sea surface temperature in the Kuroshio Extension. Can J Fish Aquat Sci. 56:973-983

Noto M, Yasuda I (2003) empirical biomass model for the Japanese sardine, *Sardinops melanostictus*, with sea surface temperature in the Kuroshio Extension. Fish Oceanogr.

12:1-9

Nurhati IS, Cobb KM, Di Lorenzo E (2011) Decadal-scale SST and Salinity Variations in the Central Tropical Pacific: Signatures of Natural and Anthropogenic Climate Change. J Clim 24 (13): 3294-3308. DOI: 10.1175/2011JCLI3852.1

Ogurtsov MG, Nagovitsyn YA, Kocharov GE, Jungner H (2002) Long-period cycles of the Sun's activity recorded in direct solar data and proxies. Solar Physics 211: 371-394

Outcalt SI, Hinkel KM, Meyer E, Brazel AJ (1997) Application of Hurst Rescaling to Geophysical Serial Data. Geographical Analysis 29 (1): 72-87

Outten SD, Esau I (2011) A link between Arctic sea ice and recent cooling trends over Eurasia. Climate Change. DOI 10.1007/s1058-011-0334-z

Overland JE, Adams JM, Bond NA (1999) Decadal Variability of the Aleutian Low and Its Relation to High-Latitude Circulation. J Clim 12: 1542-1548

Patterson RT, Prokoph A, Chang A (2004) Late Holocene sedimentary response to solar and cosmic ray activity influenced climate variability in the NE Pacific. Sedimentary Geology 172: 6784

Petoukhov V, Semenov VA (2010) A link between reduced Barents-Kara sea ice and cold winter extremes over northern continents. J Geophys Res 115(D21111). Doi:1029/2009JD013568

Pikovsky A, Rosenblum M, Kurths J (2001; reprinted 2003), Synchronization: A universal concept in nonlinear sciences. Cambridge University Press. ISBN 0 521 59285 2, 370p

Polovina JJ, Mitchum GT, Evans GT (1995) Decadal and basin-scale variation in mixed layer depth and the impact on biological production in the central and North Pacific 1960-1988. Deep-Sea Research I 42:1701-1716

Polyakov IV, Alekseev GV, Timokhov LA, Bhatt JS, Colony RL, Simmons HL, Walsh D, Walsh JE, and Zakharov VF (2004) Variability of the intermediate Atlantic water of the Arctic Ocean over the last 100 years. J Clim 16(12): 2067-2077.

Polyakov IV, Beszczynska A, Carmack EC, Dmitrenko IA, Fahrbach E, Frolov IE, Gerdes R, Hansen E, Holfort J, Ivanov VV, Johnson MA, Karcher M, Kauker F, Morison J, Orvik KA, Schauer U, Simmons HL, Skagseth O, Sokolov VT, Steele M, Timokhov LA, Walsh D, and Walsh JE (2005) One more step toward a warmer Arctic. Geophys Res Lett 32: L17605. doi:10.1029/2005GL023740

Polyakov IV, Timokhov LA, Alexeev VA, Bacon S, Dmitrenko IA, Fortier L, Frolov IE, Gascard J, Hansen E, Ivanov VV, Laxon S, Mauritzen C, Perovich D, Shimada K, Simmons HL, Sokolov VT, Steele M, Toole M (2010) Arctic Ocean Warming Contributes to Reduced Polar Ice Cap. J of Phys Ocean 40(12):2743-2756. doi:http://dx.doi.org/10.1175/2010JPO4339.1

Rayner NA, Parker DE, Horton EB, Folland CK, Alexander V, Rowell DP, Kent EC, Kaplan A (2003) Global analyses of sea surface temperature, sea ice, and night marine air temperature since the late nineteenth century. J Geophys Res 108(D14): 4407. doi:10.1029/2002JD002670

Rayner NA, Brohan P, Parker DE, Folland CK, Kennedy JJ, Vanicek M, Ansell TJ, Tett SFB (2006) Improved Analyses of Changes and Uncertainties in Sea Surface Temperature Measured In Situ since the Mid-Nineteenth Century: The HadSST2 Dataset. J of Clim 19: 446-469.

Schmittner A, Appenzeller C, Stocker TF (2000). Enhanced Atlantic freshwater export during El Nino. Geophys Res Lett 27(8):1163-1166

Shimada K, Kamoshida T, Itoh M, Nishino S, Carmack E, McLaughlin R, Zimmermann S, Proshutinsky A (2006) Pacific Ocean inflow: influence on catastrophic reduction of sea ice cover in the Arctic Ocean. Geophys Res Lett 33: L08605. doi:10.1029/2005GL025624

Sidorenkov N and Svirenko PI (1988) Diagnosis of some parameters of global water change based on the data of irregularity of the Earth Rotation Velocity. Proceedings of Academy of Science. Geography Ser., 11: 6-23. [in Russian, English summary]

Sidorenkov N and Svirenko PI (1991) Multiannual atmospheric circulation change and climate oscillation in first synoptical region. Proceedings of Hydrometcenter. 316: 93-105 [in Russian]

Sidorenkov NS (2005) Physics of the Earth's rotation instabilities. Astronomical and Astrophysical Transactions 24 (5): 425-439 DOI:10.1080/10556790600593506

Sidorenkov NS, Lutsenko OV, Bryazgin NN (2005) Variation of the mass of the sheet of Antarctica and instability of the Earth's rotation. Russian Meteorology and Hydrology 8: 5-13

Sidorenkov NS (2009) The interaction between Earth's rotation and geophysical processes. WILEY-VCH Verlag GmbH and Co. KGaA, Weinheim 305pp

Stephenson FR and Morrison LV (1984) Long-term changes in the rotation of the Earth: 700 B.C. to A.D. 1980. Philosophical Transactions of the Royal Society of London A 313 (1524):47-70. DOI: 10.1098/rsta.1984.0082

Subbotin VV (1988) On the issue of the role of sea ice in the dynamics of the climatic system of the Arctic. AARI Proc 404: 82-96 [in Russian; see Frolov et al. 2009]

Thompson DWJ and Wallace JM (2000) Annular modes in the extratropical circulation. Part I: Month-to-month variability. J Clim 13: 1000-1016

Timmermans M –L, Proshutinsky A, Krishfield RA, Perovich DK, Richter-Menge JA, Stanton TP, Toole JM (2011) Surface freshening in the Arctic Ocean's Eurasian Basin: An apparent consequence of recent change in the wind-driven circulation. Journal of Geophysical Research 116(C00D03). Doi:10.1029/2011JC006975

Tsonis AA, Swanson K, Kravtsov S (2007) A new dynamical mechanism for major climate shifts. Geophys Res Lett 34: L13705. doi:10.1029/2007GL030288

Van Loon H, Founda D, Psiloglou BE (2007) Circulation Changes on the Northern Hemisphere in Winter Associated with Trends in the Surface Air Temperature. Academy of Athens, Research Centre for Atmospheric Physics and Climatology. Publication 17: 1-29

Vangenheim GYa (1940) The long-term temperature and ice break-up forecasting. Proc State Hydrological Institute Iss. 10: 207-236 [in Russian]

Wang M, Overland JE (2009) a sea ice free summer Arctic within 30 years: Geophys Res Lett 36. L07502. doi:10.1029/2009GL037820

Wyatt MG, Kravtsov S, Tsonis AA (2012) Atlantic Multidecadal Oscillation and Northern Hemisphere's climate variability. Clim Dyn 38 (5-6): 929-949 DOI: 10.1007/s00382-011-1071-8

Wyatt MG (2012) A Multidecadal Climate Signal Propagating Across the Northern Hemisphere through Indices of a Synchronized Network. Ph.D. Dissertation. University of Colorado, Boulder, CO, 220 pp. [Available from UMI ProQuest. Publication #UMI3527373 Ann Arbor, MI.]

Wyatt MG and Peters JM (2012) A Secularly Varying Hemispheric Climate-Signal Propagation Previously Detected in Instrumental and Proxy Data Not Detected in CMIP3 Data Base. SpringerPlus 2012, 1:68 doi:10.1186/2193-1801-1-68

Yasuda I (2003) Hydrographic structure and variability in the Kuroshio-Oyashio Transition Area. Journal of Oceanography. 59: 389-402

Yasuda I, Tozuka T, Noto M, Kouketsu S (2000) Heat balance and regime shifts of the mixed layer in the Kuroshio Extension. Prog Oceanogr. 47:257-278

Zakharov VF (1997) Sea Ice in the Climate System. World Climate Research Programme. Arctic Climate System Study (ACSYS). State Research Center of the Russian Federation-Arctic and Antarctic Research Institute,Federal Service for Hydrometeorlogy and Envirnment Monitoring. St. Petersburg, Russian Federation. WMO/TD-No.782: 1-77. [Russian translated to English]

Zakharov VF (2013) Sea Ice in the Climate System, A Russian View. National Snow and Ice Data Center, Boulder, CO. Special Report #16 (same as 1997 version, with updates) http://nsidc.org/pubs/special/nsidc_special_report_15.pdf

Zhang R, Delworth TL (2005) Simulated Tropical Response to a Substantial Weakening of the Atlantic Thermohaline Circulation. J Clim 18: 1853-1860

Zhang J, Steele M, and Schweiger A (2010) Arctic sea ice response to atmospheric forcings with varying levels of anthropogenic warming and climate variability. Geophys Res Lett 37. L20505. doi:10.1020/2010GL044988

Table Captions

Table 1. Index descriptions for indices appended to original stadium-wave network

Table 2. Ice Categories: Correlations of sea ice-extent in shelf seas of the Eurasian Arctic. Seas are grouped in several ways. Each group plays a specific role in the generation and/or transmission of climate signal. Raw data smoothed 13-y. Significance levels: in red=p<1%; in blue =p< 5%.

Table 3a. Temporal Group I: correlations reflecting ocean-ice coupling. Raw data smoothed 13-y. Significance levels: in red=p<1%; in blue = p<5%.

Table 3b. Temporal Group I: correlations reflecting relationship between anomalies of Pacific-centered circulations and Group I indices. Raw data smoothed 13-y. Significance levels: in red=p<1%; in blue = p<5%.

Table 3c. Temporal Group I: correlations of Proxies with Group I indices. Raw data smoothed 13-y. Significance levels: in red=p<1%; in blue = p<5%.

Table 4. Temporal Group II: correlations reflecting ice-atmosphere coupling. Significance levels: in red=p<1%; in blue = p<5%.

Table 5a. Temporal Group III: Correlations between anomaly trends of sea ice extent and associated wind patterns with Pacific-centered ocean/atmosphere circulations. Significance level: in red=p<1%.

Table 5b. Temporal Group III: Japanese Sardine Proxy with Pacific-centered circulation-pattern indices. Significance level: in red=p<1%.

Table 6a. Temporal Group IV: anomaly trends of sea ice extent and related circulation patterns correlate with temperature. Significance levels for correlations: in red=p<1%; in blue = p<5%.

Table 6b. Temporal Group IV: ngLOD proxy with wind anomaly and Arctic T. Significance levels: in red=p<1%; in blue =p< 5%.

Table 6c. Temporal Group IV: correlation shows relationship of Arctic temperature with sea ice in WIE. Significance Levels: in red=p<1%; in blue = p<5%.

Figure Captions

Fig. 1. Arctic Ocean and marginal seas used in this study (1-6 in this study (shaded in gray)): 1) Greenland Sea, 2) Barents Sea, 3) Kara Sea, 4) Laptev Sea, 5) East Siberian Sea, 6) Chukchi Sea. Categories of Seas include: NEB = 1&2; ArcSib = 3-6; WIE = 1-3; EIE = 4-6; and TIE = 1-6. [Also shown: 7) Beaufort Seas, 8) Baffin Bay, 9) Hudson Bay, and 10) the Norwegian Sea.] Adapted with permission from: Frolov et al. 2009.

Fig. 2. **a**) Plot of MSSA normalized RCs 1&2 of Original 20^{th}-century Stadium-Wave (adapted from Wyatt et al. 2011 (WKT)). Note: NHT and AMO are negative; **b**) M-SSA spectrum of a. Error bars in b are based on North et al. (1982) criterion, with the number of degrees-of-freedom set to 40, based on decorrelation time of ~2.5 years. Red-dashed lines in panel (b) represent the 95% spread of M-SSA eigenvalues based on 100 simulations of the 8-valued red-noise model (1), which assumes zero true correlations between the members of the eight-index set.

Fig. 3. Annotated Expanded ‘Stadium Wave’ shows 20^{th}-century signal propagation through a 15-index-member network. Selected indices are a sub-set of a broader network. Four clusters of indices are highlighted (+/- I through IV). Each cluster is termed a “Temporal Group”. Peak values of Group indices represent stages of climate-regime evolution. Each is discussed individually (see text) and plotted (Figures 7-10). Plotted indices are normalized reconstructed components of M-SSA modes 1&2.

Fig. 4. M-SSA spectrum of expanded stadium-wave network shown in Figure 3. Error bars are based on North et al. (1982) criterion, with the number of degrees-of-freedom set to 40, based on decorrelation time of ~2.5 years. Red-dashed lines in panel represent the 95% spread of M-SSA eigenvalues based on 1000 simulations of the 15-valued red-noise

model (1), which assumes zero true correlations between the members of the 15-index set.

Fig. 5. Channel-fraction variance due to M-SSA leading modes 1&2. Values indicate the amount of an index's variability that is due to the stadium-wave signal. Indices represent Groups: I [WIE, AMO, GB]; II [ArcSib, AT, NAOw, NPGO]; III [EIE, NINO, JS, PDO, ALPI]; IV [ArcticT, ngLOD, and NHT].

Fig. 6. Raw data plots: 20^{th}-century relationships among anomaly trends of *negatively* signed Pacific circulations (e.g. ngPCI and -csPDO) and the trend of ngAMO. "Change-points" of anomaly trends indicate endings of intervals dominated by either positive or negative anomalies. Change-points of Pacific anomaly trends co-occur with extrema of the AMO curve. Plotted indices: raw data. AMO smoothed 13y; ngPCI and-csPDO are not smoothed.

Fig. 7. Temporal Group I: characterized by ocean-ice coupling, with focus of activity in the Atlantic sector. Peak values center on ~1918 and 1976; minimum values in the 20^{th} century center on ~1942. Associated proxies are the G. *bulloides* and ngDipole. Plotted indices are normalized reconstructed components of M-SSA modes 1&2.

Fig. 8. Temporal Group II: characterized by ice-atmosphere coupling. Sea ice extent in Russian Arctic (ArcSib) and related large-scale wind patterns co-vary with peak values centered on ~1923 and ~1982; minimum values center on ~1950. Associated proxy is the NPGO proxy. Plotted indices are normalized reconstructed components of M-SSA modes 1&2.

Fig. 9. Temporal Group III: Pacific centered atmospheric, oceanic, and ice indices. Indices reach maximum values ~1930 and 1990 and minimum values ~1904 and ~1964. Associated

proxy is the Japanese Sardine index. Plotted indices are normalized reconstructed components of M-SSA modes 1&2.

Fig. 10. Temporal Group IV: culmination of anomaly trends of sea ice extent, associated basin-scale winds, and temperature extrema. Maximum values center on ~1938 and ~1998; minima ~1910 and ~1971. Note: csArcSib leads other indices ~3y. Associated proxy is ngLOD. Plotted indices are normalized reconstructed components of M-SSA modes 1&2.

Fig. 11. Schematic reflects index relationships at each stage of climate-regime evolution. Vertical lines represent peak values of indices for each Temporal Group (refer to Figures 7-10). Dates for these maxima are indicated along the bottom. Four Temporal Groups are represented, each by one index. They are listed in the left column. Arrows indicate index trends between 'stages' (or peaks of Temporal-Group indices). Red arrows indicate an increasing trend. Blue arrows a decreasing one. *Note*: AMO sign is positive in chart. See text for explanation.

Fig. 12. Stadium-Wave 'Mechanism': schematic of simplified version of stadium-wave-signal propagation through the ocean-ice-atmospheric network and its influence on climate-regime evolution. Roman numerals indicate processes related to Temporal Groups I through IV. Numbers in red (blue) indicate increasing (decreasing) Arctic and Northern Hemisphere temperatures. (MTG = meridional temperature gradient; WAA = warm air advection)

Fig. 13. Stadium-Wave 'Wheel': Temporal Group indices are displayed in 'wheel' segments. Rings contain indices according to system: WKT indices are in the grey ring; ice indices fill the yellow ring; wind and wind-related indices, the blue-green ring; and proxies populate the outer green ring. Refer to text on how to read 'the wheel'.

Table 1. Index descriptions for indices appended to original stadium-wave network

Index/Acronym	**Reference/Data source**	**Description/General Information**
(AO) Arctic Oscillation	Thompson and Wallace 2000 www.atmos.colostate.edu or http://jisao.washington.edu/ao#data	Leading EOF of SLP poleward 20N
(GB) Globigerina.bulloides	Black et al. 1999 (record updated to 2009 (personal communication)	*G. bulloides* Cariaco Basin (ITCZ proxy)
(JS) Japanese Sardine	Klyashtorin and Lyubushin (2007); Kawasaki 1994;Klyashtorin 1998 (and personal communication)	Outbursts off coast of Japan. Related to +PDO
(ngLOD) Earth's Rotational-Rate	Sidorenkov (2005; 2009) and personal communication http://hpiers.obspm.fr/eop-pc/earthor/ut1lod/lod-1623.html	low-frequency-variability of negative length-of-day
(NPGO) SST proxy	Nurhati et al. (2011): +NPGO ~ **-**SSTs of coral-based Sr/Ca proxy (R = -0.85)	Coral Sr/Ca SST proxy 162ºW, 6ºN
(Arctic T) Arctic surface temperature anomalies	Frolov et al. (2009) personal communication Smolyanitsky http://wdc.aari.ru/datasets/d0005/txt	Mean annual surface air temperature (SAT): 70 to 85ºN for 1900-2007
(Grnlnd) Greenland sea-ice extent	Frolov et al. (2009) also available at: http://wdc.aari.ru/datasets/d0005/txt	Mean August values **~15ºW-15ºE**
(Barents) Barents sea-ice extent	Frolov et al. (2009) also available at: http://wdc.aari.ru/datasets/d0005/txt	Mean August values **~15ºE-60ºE**
(NEB) North European Basin	Frolov et al (2009)	Mean August values: (Greenland + Barents ice)
(Kara) Kara sea-ice extent	Frolov et al. (2009) also available at: http://wdc.aari.ru/datasets/d0005/txt	Mean August values ~60ºE-100ºE
(WIE) [Grn, Bar, Kara] West Ice Extent	Frolov et al. (2009)	Mean August values: ~15ºW~100ºE
(Laptv) Laptev sea-ice extent	Frolov et al. (2009) also available at: http://wdc.aari.ru/datasets/d0005/txt	Mean August values: ~100ºE-140ºE
(E.Sib) East Siberian SIE	Frolov et al. (2009) also available at: http://wdc.aari.ru/datasets/d0005/txt	Mean August values: ~140ºE--~180º
(Chuk) Chukchi sea-ice extent	Frolov et al. (2009) also available at: http://wdc.aari.ru/datasets/d0005/txt	Mean August values: ~180-155ºW
(EIE) [Lap,ESib, Chuk] East Ice Extent	Frolov et al. (2009)	Mean August values:100ºE --~155ºW
(ArcSib) Arctic Seas of Siberia [Kara EIE]	Frolov et al. (2009)	Mean August values: Kara + EIE
(TIE) WIE + EIE Total Ice Extent :	Frolov et al. (2009)	Mean August values: 15ºW - 155ºW
(PCI) Pacific Circulation Indx	Beamish et al. 1998; King et al. 1998	Anomaly trend of Pacific atmospheric circulation
(Dipole) proxy A-ITCZ Atlantic SST Dipole	Keenlyside et al. 2008	SSTavg (60 to 10W, 40to 60N)-(50to0W, 40to60S);

Table 2. Ice Categories: Correlations of sea ice-extent in shelf seas of the Eurasian Arctic. Seas are grouped in several ways. Each group plays a specific role in the generation and/or transmission of climate signal. Raw data smoothed 13-y. Significance levels: in red=p<1%; in blue =p< 5%.

Indices	NEB	WIE	TIE	Arc_Sib	EIE
Greenland	0.95	0.90	0.65		
Barents	0.98	0.94	0.66		
Kara	0.70	0.87	0.94	0.87	
WIE	0.96	1.0	0.84	0.57	
TIE	0.68	0.84	1.0	0.91	
Laptev				0.70	0.85
East_Sib				0.55	0.91
Chukchi				0.63	0.91
EIE				0.69	1.0

Table 3a. Temporal Group I: correlations reflecting ocean-ice coupling. Raw data smoothed 13-y. Significance levels: in red=p<1%; in blue = p<5%.

Indices	NEB	WIE
ngAMO	0.88	0.89

Table 3b. Temporal Group I: correlations reflecting relationship between anomalies of Pacific-centered circulations and Group I indices. Raw data smoothed 13-y. Significance levels: in red=p<1%; in blue = p<5%.

Indices	NEB	WIE	ngAMO	ngPCI
ngPCI	0.84	0.92	0.93	1.0
cs(ng)NPO	0.82	0.89	0.93	0.96
cs(ng)PDO	0.73	0.83	0.86	0.95
cs(ng)ALPI	0.72	0.84	0.83	0.95

Table 3c. Temporal Group I: correlations of Proxies with Group I indices. Raw data smoothed 13-y. Significance levels: in red=p<1%; in blue = p<5%.

Indices	GB	ngDipole
Greenland	0.78	0.79
Barents	0.72	0.70
NEB	0.77	0.76
WIE	0.78	0.75
ngAMO	0.88	0.90
ngPCI	0.80	0.79
Ng_csPDO	0.85	0.83
Ng_csNPO	0.83	0.81

Table 4. Temporal Group II: correlations reflecting ice-atmosphere coupling. Significance levels: in red=p<1%; in blue = p<5%.

Indices	TIE	ArcSib	Kara ice	Chukchi ice	Laptev ice
AT	0.75	0.76	0.70	0.57	
NPGO	0.56	0.69		0.62	0.60

Table 5a. Temporal Group III: Correlations between anomaly trends of sea ice extent and associated wind patterns with Pacific-centered ocean/atmosphere circulations. Significance level: in red=p<1%.

Indices	csWIE	csTIE	csNEB	csArc_Sib	csKara	csAT
NPO	0.83	0.86	0.77	0.81	0.87	0.77
ALPI		0.79		0.81	0.77	0.76
PDO		0.83		0.82	0.81	

Table 5b. Temporal Group III: Japanese Sardine Proxy with Pacific-centered circulation-pattern indices. Significance level: in red=p<1%.

Indices	JS
NPO	0.69
PDO	0.80
ALPI	0.70

Table 6a. Temporal Group IV: anomaly trends of sea ice extent and related circulation patterns correlate with temperature. Significance levels for correlations: in red=p<1%; in blue = p<5%.

Indices	Arctic Temperature	NHT	csArcSib
csNAOw	0.81		
csAOw	0.86		
csNPGO	0.79		
csAT (aka ACI)	0.92	0.81	0.88
csNINO	0.85	0.83	
csArcSib	0.77		

Table 6b. Temporal Group IV: ngLOD proxy with wind anomaly and Arctic T. Significance levels: in red=p<1%; in blue =p< 5%.

Indices	ngLOD
csAT (aka ACI)	0.83
ArcticT	0.76

Table 6c. Temporal Group IV: correlation shows relationship of Arctic temperature with sea ice in WIE. Significance Levels: in red=p<1%; in blue = p<5%.

Indices	Arctic Temperature
NEB	-0.78
WIE	-0.76

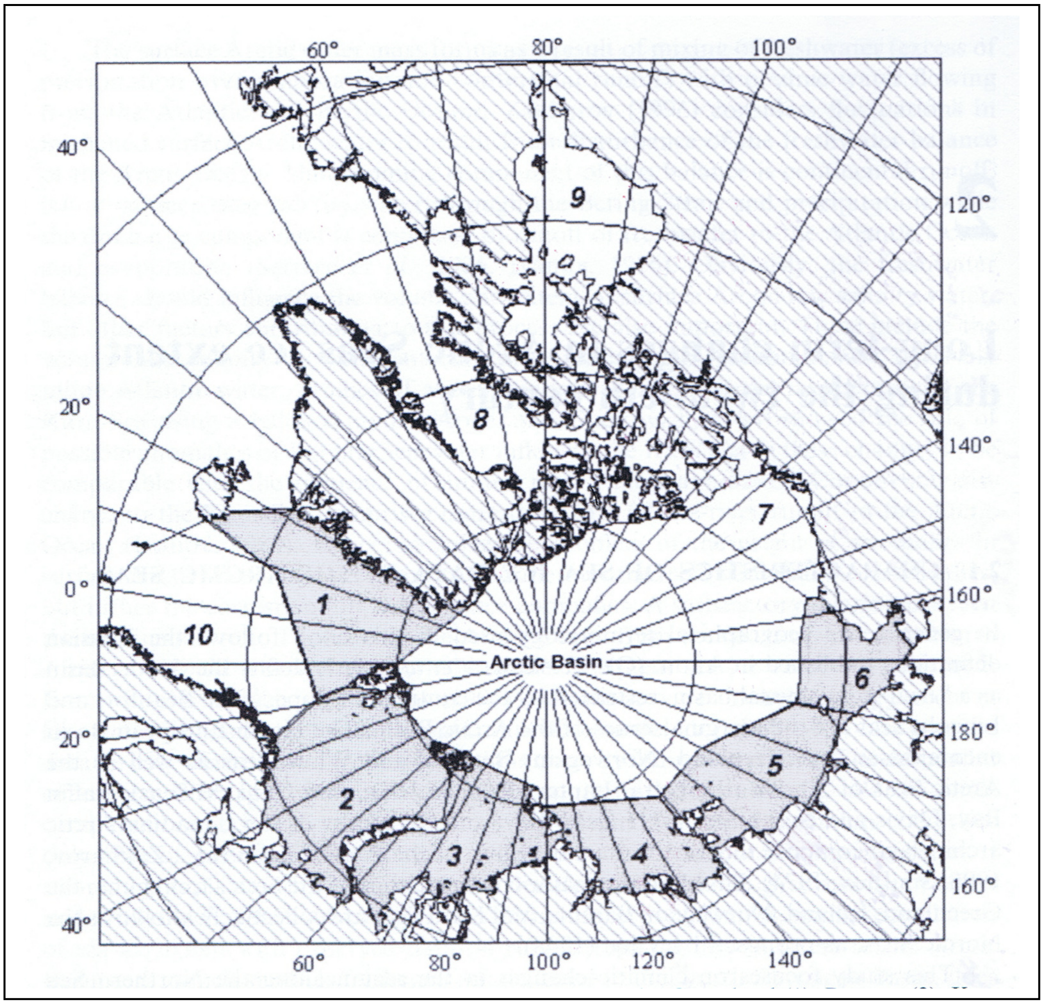

Fig. 1. Arctic Ocean and marginal seas used in this study (1-6 in this study (shaded in gray)): 1) Greenland Sea, 2) Barents Sea, 3) Kara Sea, 4) Laptev Sea, 5) East Siberian Sea, 6) Chukchi Sea. Categories of Seas include: NEB = 1&2; ArcSib = 3-6; WIE = 1-3; EIE = 4-6; and TIE = 1-6. [Also shown: 7) Beaufort Seas, 8) Baffin Bay, 9) Hudson Bay, and 10) the Norwegian Sea.] Adapted with permission from: Frolov et al. 2009.

a)

b)

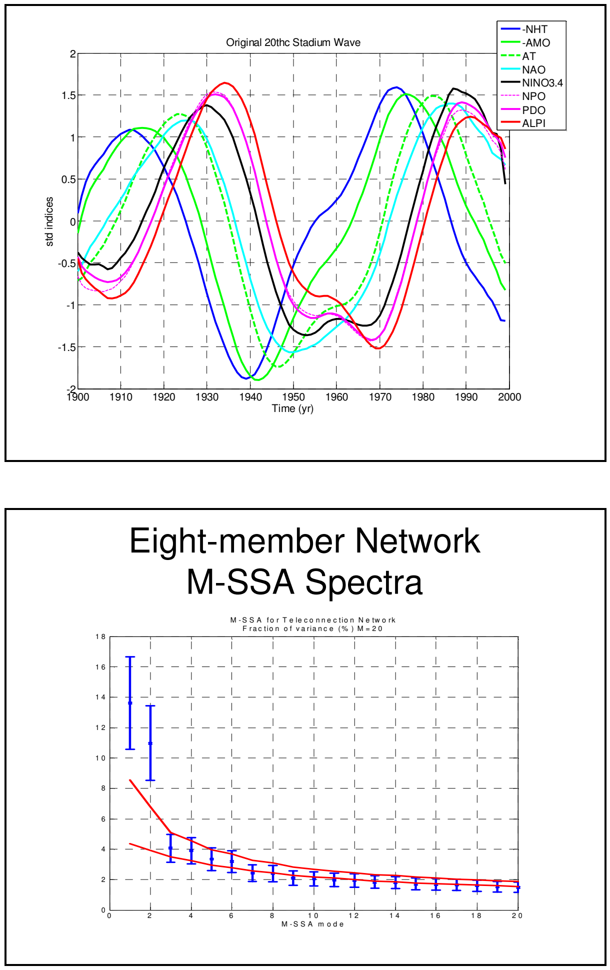

Fig. 2. a) Plot of MSSA normalized RCs 1&2 of Original 20th-century Stadium-Wave (adapted from Wyatt et al. 2011 (WKT)). Note: NHT and AMO are negative; **b**) M-SSA spectrum of a. Error bars in b are based on North et al. (1982) criterion, with the number of degrees-of-freedom set to 40, based on decorrelation time of ~2.5 years. Red-dashed lines in panel (b) represent the 95% spread of M-SSA eigenvalues based on 100 simulations of the 8-valued red-noise model (1), which assumes zero true correlations between the members of the eight-index set.

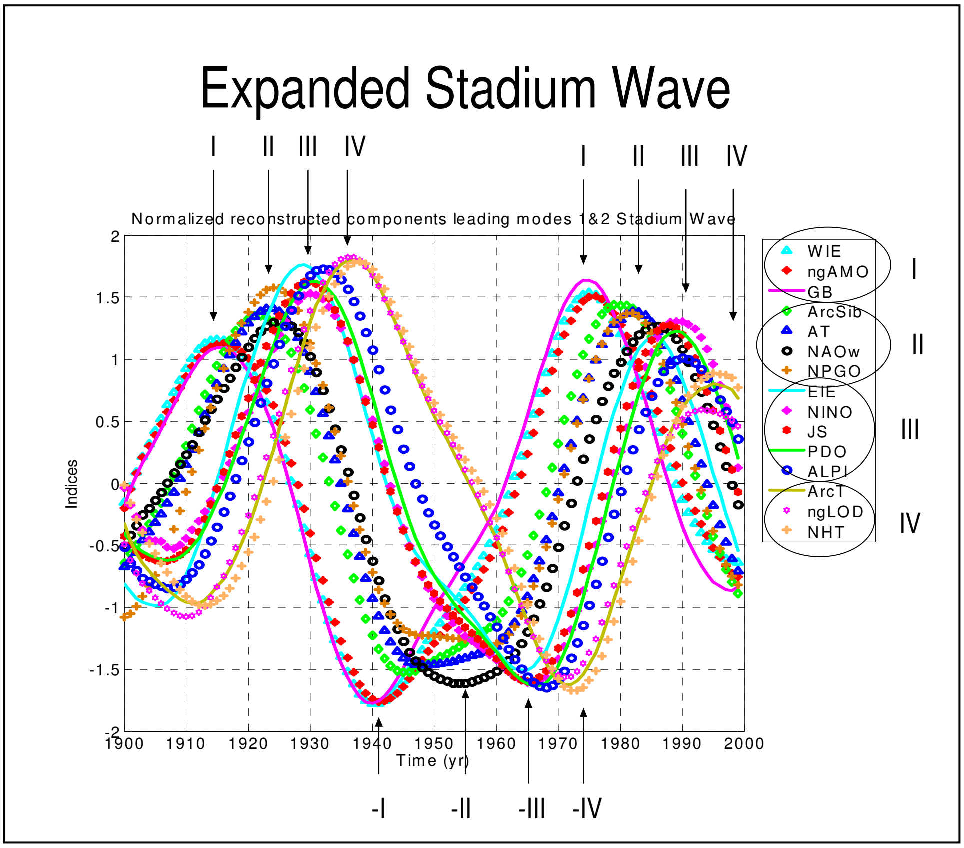

Fig. 3. Annotated Expanded 'Stadium Wave' shows 20th-century signal propagation through a 15-index-member network. Selected indices are a sub-set of a broader network. Four clusters of indices are highlighted (+/- I through IV). Each cluster is termed a "Temporal Group". Peak values of Group indices represent stages of climate-regime evolution. Each is discussed individually (see text) and plotted (Figures 7-10). Plotted indices are normalized reconstructed components of M-SSA modes 1&2.

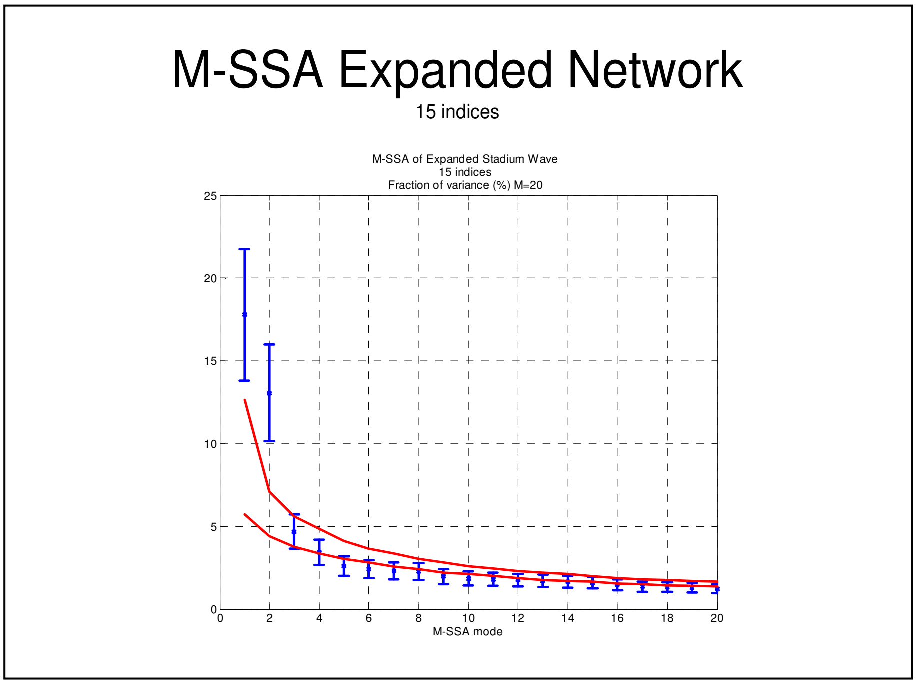

Fig. 4. M-SSA spectrum of expanded stadium-wave network shown in Figure 3. Error bars are based on North et al. (1982) criterion, with the number of degrees-of-freedom set to 40, based on decorrelation time of ~2.5 years. Red-dashed lines in panel represent the 95% spread of M-SSA eigenvalues based on 1000 simulations of the 15-valued red-noise model (1), which assumes zero true correlations between the members of the 15-index set.

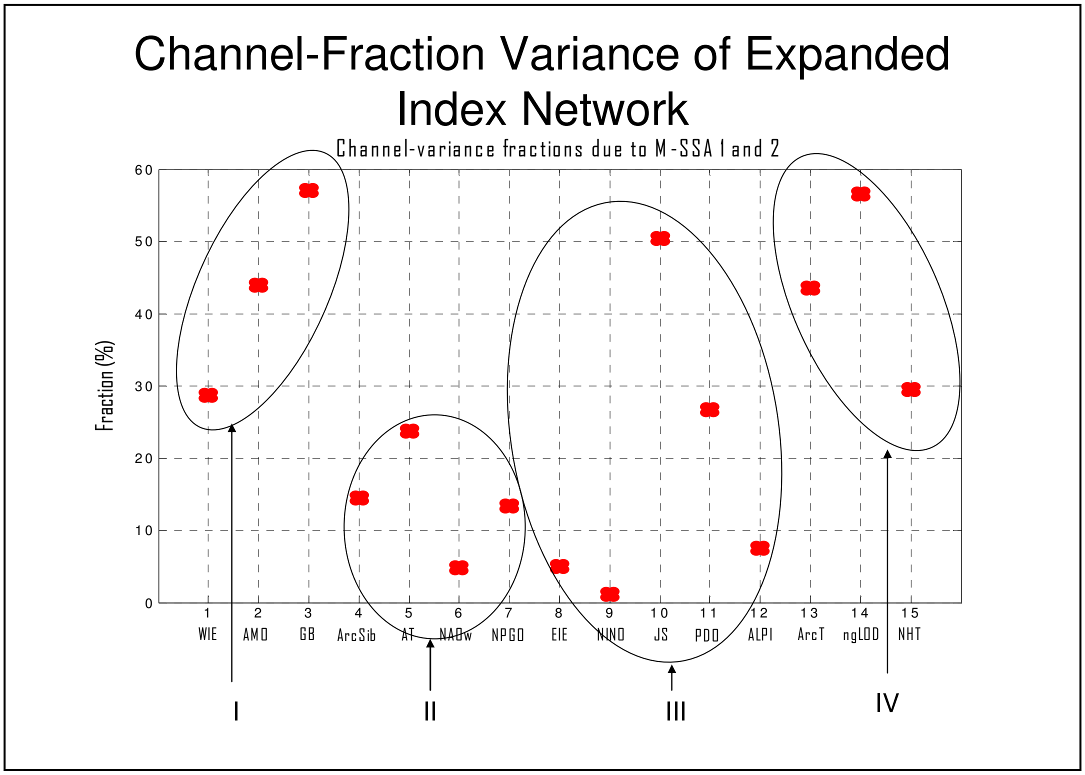

Fig. 5. Channel-fraction variance due to M-SSA leading modes 1&2. Values indicate the amount of an index's variability that is due to the stadium-wave signal. Indices represent Groups: I [WIE, AMO, GB]; II [ArcSib, AT, NAOw, NPGO]; III [EIE, NINO, JS, PDO, ALPI]; IV [ArcticT, ngLOD, and NHT].

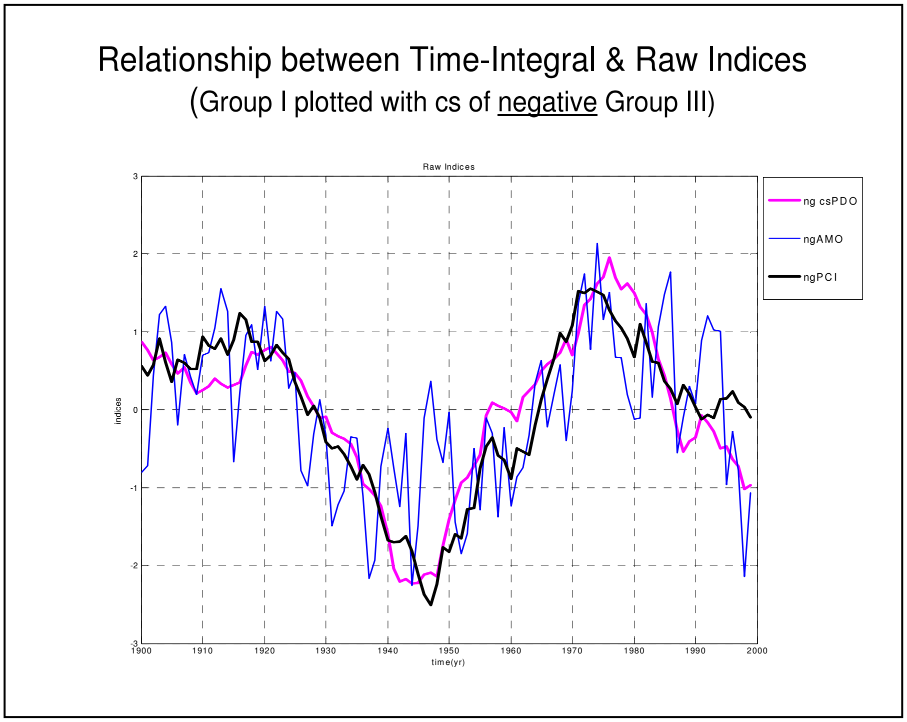

Fig. 6. Raw data plots: 20th-century relationships among anomaly trends of *negatively* signed Pacific circulations (e.g. ngPCI and -csPDO) and the trend of ngAMO. "Change-points" of anomaly trends indicate endings of intervals dominated by either positive or negative anomalies. Change-points of Pacific anomaly trends co-occur with extrema of the AMO curve. Plotted indices: raw data. AMO smoothed 13y; ngPCI and-csPDO are not smoothed.

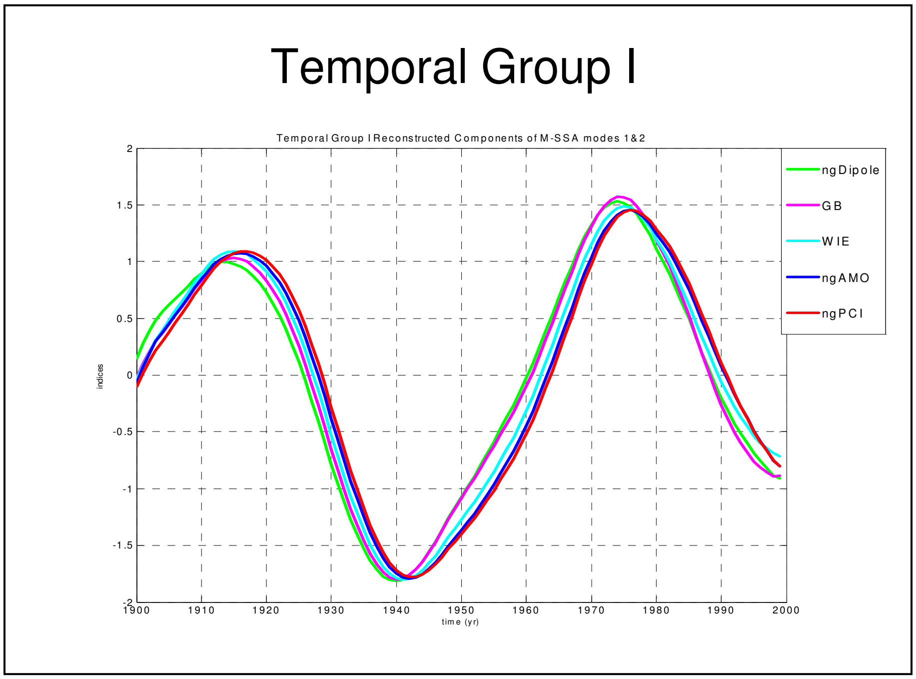

Fig. 7. Temporal Group I: characterized by ocean-ice coupling, with focus of activity in the Atlantic sector. Peak values center on ~1918 and 1976; minimum values in the 20th century center on ~1942. Associated proxies are the G. *bulloides* and ngDipole. Plotted indices are normalized reconstructed components of M-SSA modes 1&2.

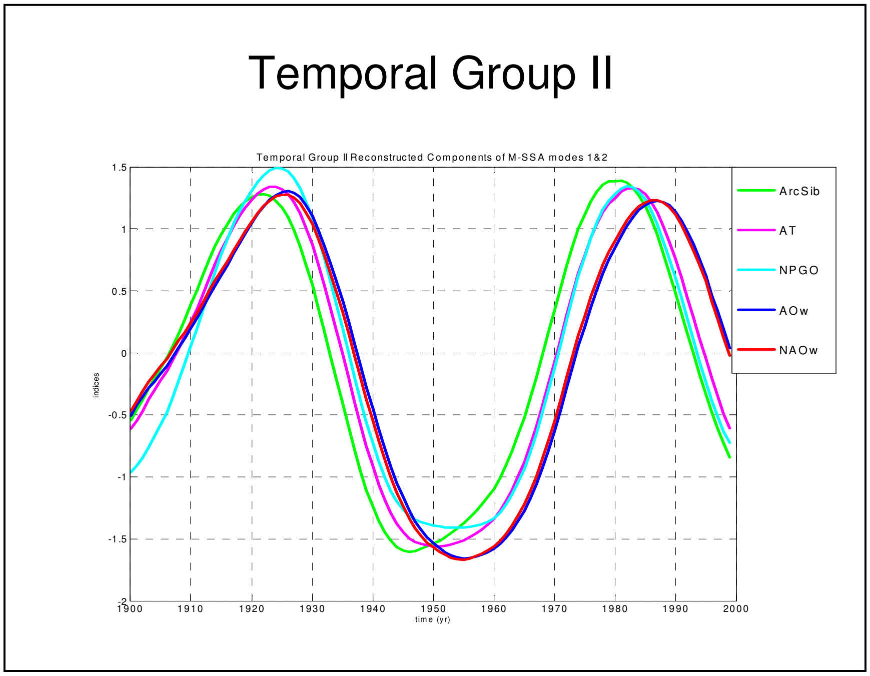

Fig. 8. Temporal Group II: characterized by ice-atmosphere coupling. Sea ice extent in Russian Arctic (ArcSib) and related large-scale wind patterns co-vary with peak values centered on ~1923 and ~1982; minimum values center on ~1950. Associated proxy is the NPGO proxy. Plotted indices are normalized reconstructed components of M-SSA modes 1&2.

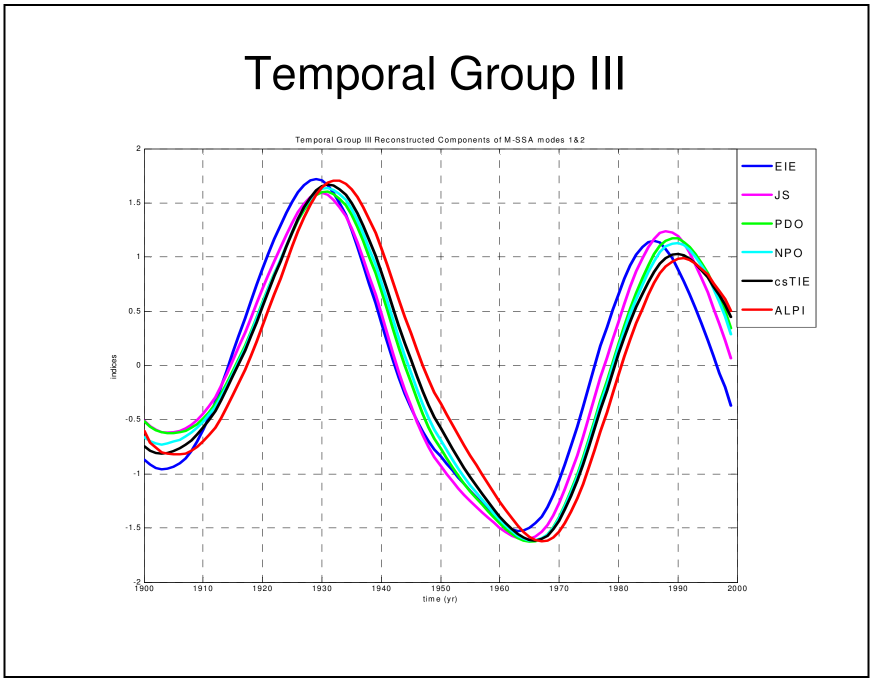

Fig. 9. Temporal Group III: Pacific centered atmospheric, oceanic, and ice indices. Indices reach maximum values ~1930 and 1990 and minimum values ~1904 and ~1964. Associated proxy is the Japanese Sardine index. Plotted indices are normalized reconstructed components of M-SSA modes 1&2.

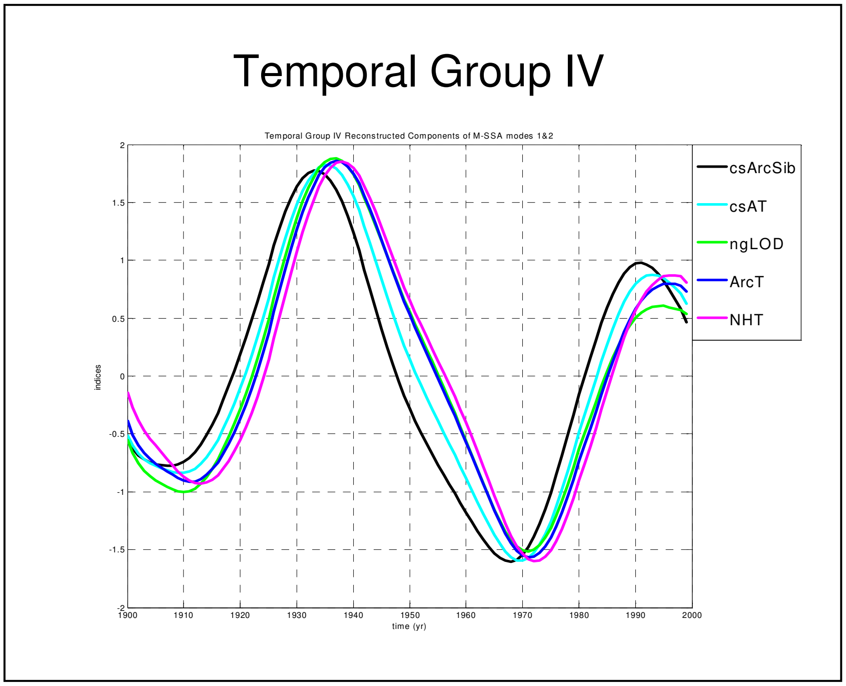

Fig. 10. Temporal Group IV: culmination of anomaly trends of sea ice extent, associated basin-scale winds, and temperature extrema. Maximum values center on ~1938 and ~1998; minima ~1910 and ~1971. Note: csArcSib leads other indices ~3y. Associated proxy is ngLOD. Plotted indices are normalized reconstructed components of M-SSA modes 1&2.

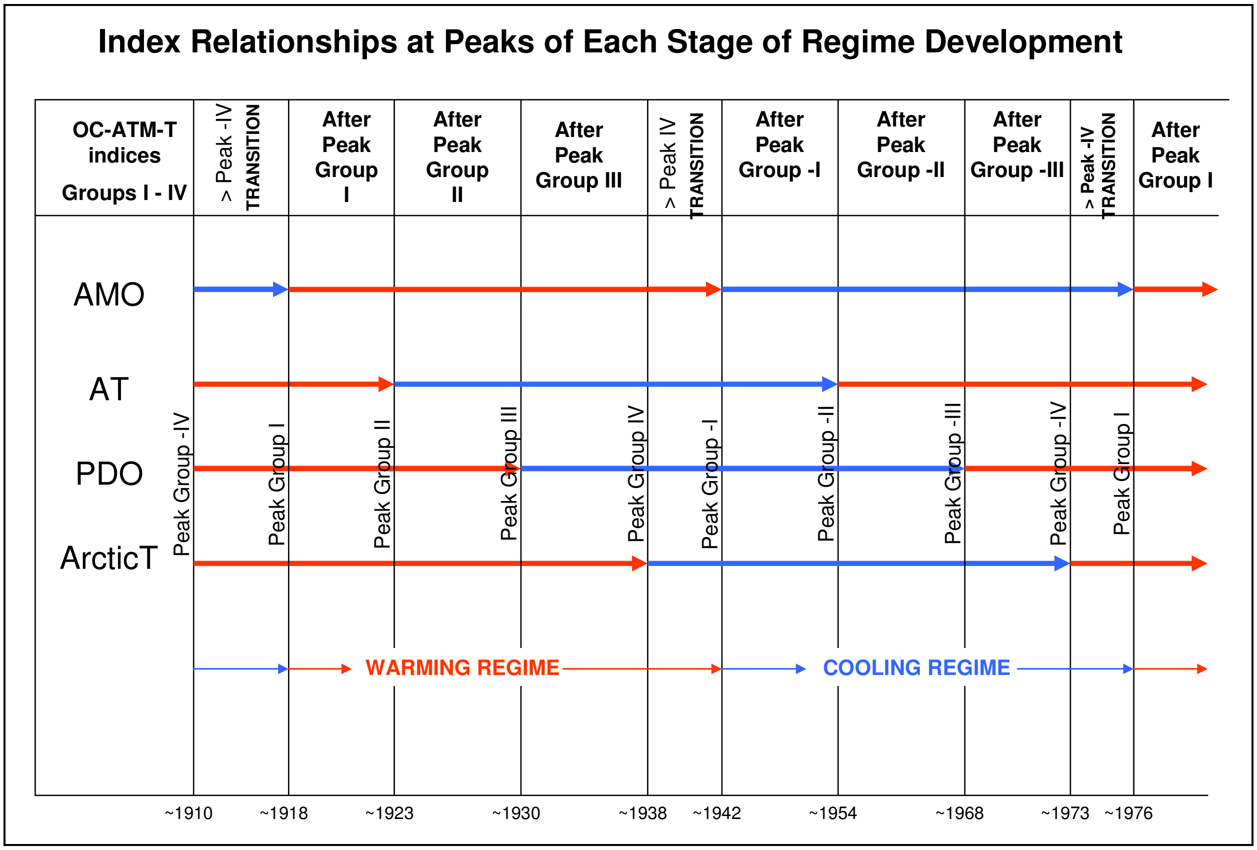

Fig. 11. Schematic reflects index relationships at each stage of climate-regime evolution. Vertical lines represent peak values of indices for each Temporal Group (refer to Figures 7-10). Dates for these maxima are indicated along the bottom. Four Temporal Groups are represented, each by one index. They are listed in the left column. Arrows indicate index trends between 'stages' (or peaks of Temporal-Group indices). Red arrows indicate an increasing trend. Blue arrows a decreasing one. *Note*: AMO sign is positive in chart. See text for explanation.

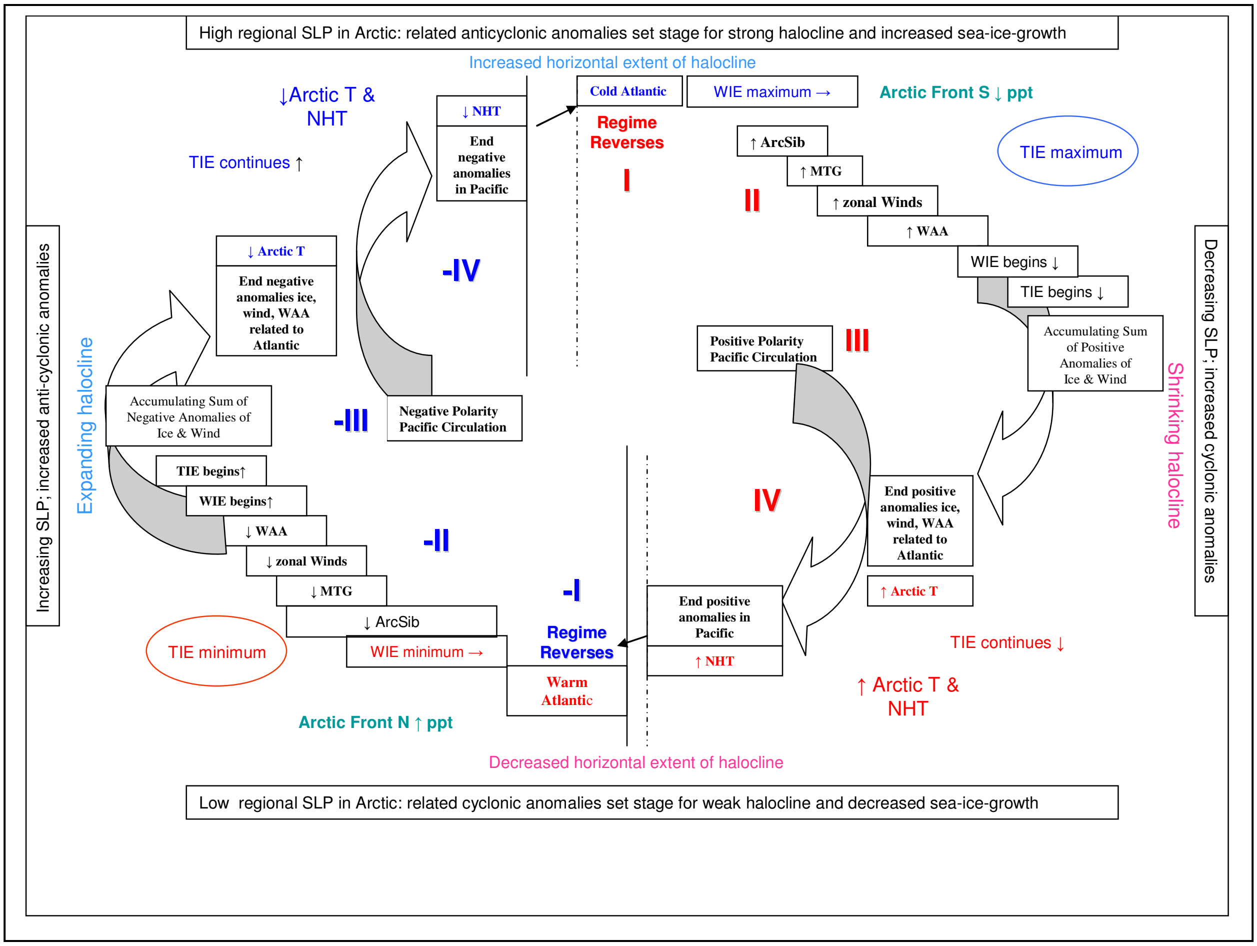

Fig. 12. Stadium-Wave 'Mechanism': schematic of simplified version of stadium-wave-signal propagation through the ocean-ice-atmospheric network and its influence on climate-regime evolution. Roman numerals indicate processes related to Temporal Groups I through IV. Numbers in red (blue) indicate increasing (decreasing) Arctic and Northern Hemisphere temperatures. (MTG = meridional temperature gradient; WAA = warm air advection)

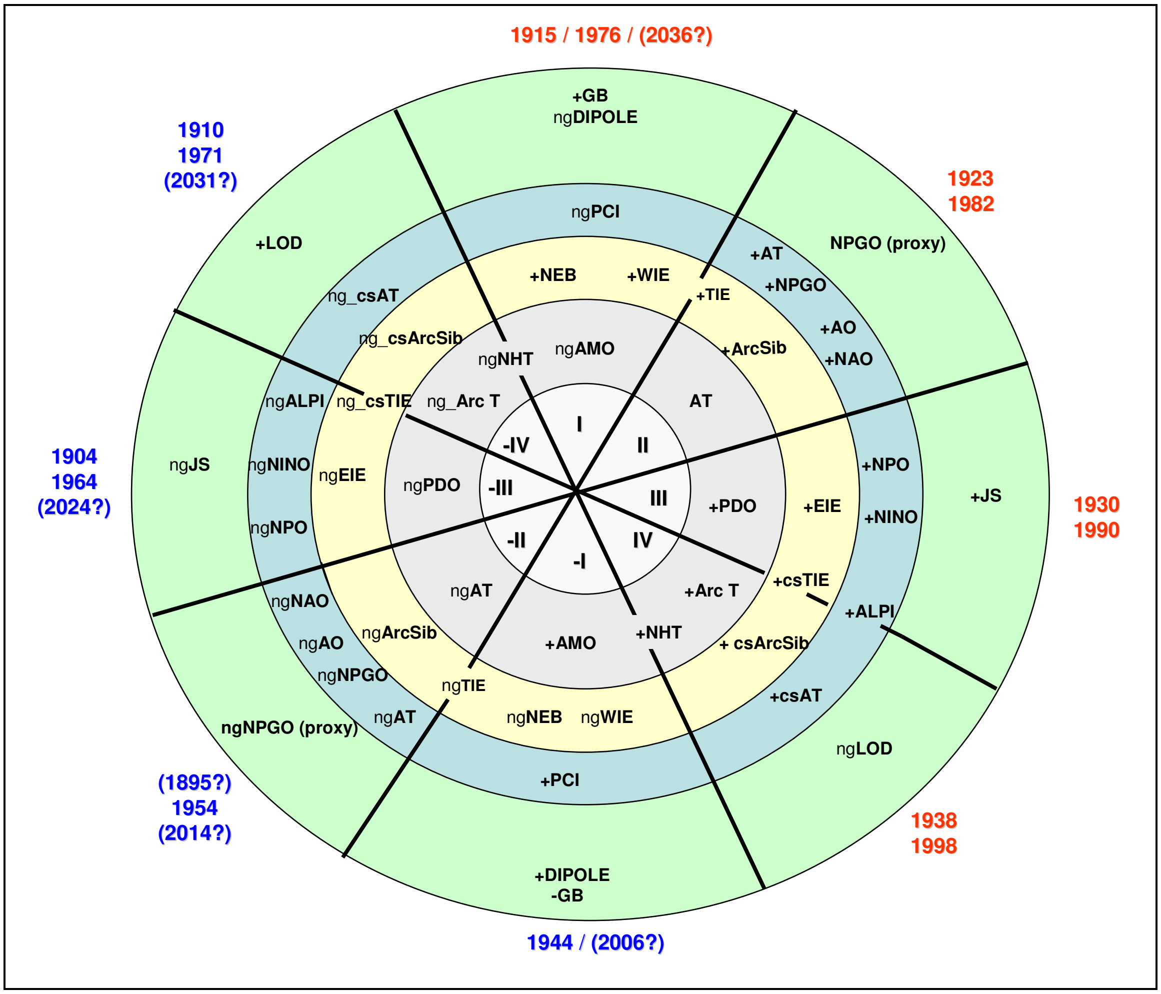

Fig. 13. Stadium-Wave 'Wheel': Temporal Group indices are displayed in 'wheel' segments. Rings contain indices according to system: WKT indices are in the grey ring; ice indices fill the yellow ring; wind and wind-related indices, the blue-green ring; and proxies populate the outer green ring. Refer to text on how to read 'the wheel'.